STUDY OF FLUID FLOW AND CAVITATION INSIDE TORQUE CONVERTERS

STUDY OF FLUID FLOW AND CAVITATION INSIDE TORQUE CONVERTERS

By

DI CHUANG, B.ENG.

A Thesis
Submitted to the School of Graduate Studies
in Partial Fulfillment of the Requirements
for the Degree
Master of Applied Science

McMaster University

MASTER OF APPLIED SCIENCE (2008)	McMaster University
(Mechanical Engineering)	Hamilton, Ontario

TITLE:	Study of Fluid Flow and Cavitation Inside Torque Converters
AUTHOR:	Di Chuang, B.Eng. (McMaster University)
SUPERVISOR:	Dr. Mohamed S. Hamed (McMaster University)
NUMBER OF PAGES:	xv, 91

ABSTRACT

Cavitation inside an automotive torque converter running at various pump speeds was simulated by using the Computational Fluid Dynamics (CFD) commercial package ANSYS-CFX 10.0/11.0. The numerical solution obtained for the case with no cavitation was used as an initial condition for the case of flow with cavitation to accelerate convergence. The converter was initially modeled using several grid sizes to evaluate the effect of grid density on the numerical solution and to select the optimum grid size for subsequent simulations. Comparison of CFD to actual test results demonstrates that the cavitation model built in the commercial code, which was developed by Zwart et. al. (2004) based on the simplified Rayleigh-Plesset equation of bubble dynamics, does not capture the full effect of cavitation inside the converter. Modifications to this model have been investigated in this study. The effect of the variation of the automotive transmission oil vapor pressure due to the rise in temperature during normal operating conditions was also investigated and found not to cause any significant change to the area of vapor formation, and hence did not have a significant effect on the converter performance. Values of the empirical coefficients of the cavitation model had to be modified in order for the model to capture the full effect of cavitation on the performance of the converter operating at high pump speeds. Results showed a much larger area of vapor over the converter stator and traces of vapor appeared inside the pump, and turbine blades. With these modifications, the model produced results in better agreement with the available experimental data. Moreover, simulations have been carried out in both steady and transient states using various turbulence models available in CFX10.0/11.0 in order to evaluate the effect of the choice of turbulence models on cavitation prediction.

ACKNOWLEDGEMENTS

First of all, I would like to appreciate my supervisor, Dr. Mohamed Hamed, for his valuable advice and generous support to my study and living in Canada. His strong academic background and industrial experience helped me to complete this work. Besides, I do appreciate GM as the sponsor of this project. I also feel thankful to Doctor Candidate Alaa Eldin Khafagy for helping me establish my simulation environment, and so to my dearest lab mates, Deepayan, George, Danish, Salam, Nasim, Ramin, Charles, and Cathy, who have never hesitated to help me. Last but not least, I want to delicate this work to my wonderful parents and wife, Mrs. Hui Feng, Mr. Kai Chuang, and Mrs. Yu Liu. Their endless love and encouragement have always been the headspring of my power and the home of my soul.

TABLE OF CONTENTS

LIST OF FIGURES

LIST OF TABLES

LIST OF SYMBOLS

$\overline{U}$ = Time averaged velocity in x direction

u = Fluctuating velocity in x direction

Re = Reynolds number

Ω = Rotational speed

T_p = Torque on the pump

T_t = Torque on the turbine

η = Efficiency of the torque converter

R = Bubble radius

σ = Surface tension of the liquid

P_v = Saturated vapor pressure

P_∞ = Pressure of the liquid surrounding the bubble

ρ = Fluid density

μ = Dynamic viscosity

μ_t = Dynamic turbulent viscosity

k = Turbulent kinetic energy ($\equiv \frac{1}{2}\overline{u_i u_i}$)

U_i = Velocity in x_i direction

$\overline{uv}, \overline{uw}$ = Shear stresses

$\overline{u_i u_j}$ = Reynolds stress tensor

U = Instantaneous velocity in x direction

V = Instantaneous velocity in y direction

W = Instantaneous velocity in z direction

$\overline{u^2}, \overline{v^2}, \overline{w^2}$ = Normal stresses

δ = Boundary layer thickness; half channel height

ε = Dissipation

κ = wave number; von Karman constant (=0.41)

ν = Kinematic viscosity

ω = specific dissipation ($\propto \varepsilon / k$)

P_k = Generation of turbulent kinetic energy due to the mean velocity gradients

$C_{\varepsilon 1}$, $C_{\varepsilon 2}$,

σ_k, = Model constants for the k-ε turbulence model

σ_ε, $C\mu$

β', α, β,

= Model constants for the k-ω turbulence model

σk, $\sigma\omega$

$\tilde{\nu}$ = Turbulent kinematic viscosity

G_ν = Production of turbulent viscosity

Y_ν = Destruction of turbulent viscosity

C_{b1}, C_{b2},

$\sigma_{\tilde{\nu}}$, $C_{\nu 1}$,

= Model constants for Spalart-Allmaras turbulence model

C_{w1}, C_{w2},

C_{w3}

$f_{\nu 1}$ = Viscous damping function

σk, $\sigma\omega$, γ, β, β^* = Model constants for the SST turbulence model

F_1, F_2 = Blending function

Pr = Prandtl number

Prt = Turbulent prandtl number

ρ_α = Density of phase α

u_i = Cartesian velocity components

$\dot{S}_\alpha$ = Mass generation rate of phase α

ρ_m = Volume-weighted mixture of density

g_i = Acceleration due to gravity

τ_{ji} = Stress tensor

μ_m = volume-weighted mixture of viscosity

P_{Go} = Initial gas pressure inside the bubble

R_0 = Initial bubble radius at time t = 0

K-factor = Performance parameter, $K_f = \Omega / \sqrt{T_p}$

C_{vap} = Vaporization coefficient

C_{cond} = Condensation coefficient

Chapter 1 Introduction & Literature Review

1.1. Torque converter (Ofria, 2000)

A torque converter is a large circle shaped device which is mounted between the engine and the transmission. A torque converter is usually consists of three elements that work together to transmit power from the engine to the transmission. The three elements of the torque converter are the Pump, the Stator, and the Turbine. (See figure 1.1). The pump is mounted directly to the converter housing which in turn is bolted directly to the engine's crankshaft and runs at the engine speed. The stator is mounted to a one-way clutch so that it can spin freely in just one direction but not the other. The turbine is inside the housing and is directly mounted to the input shaft of the transmission, providing power to move the vehicle. Each of the three elements has internally mounted fins to accurately direct the flow of transmission oil through the torque converter.

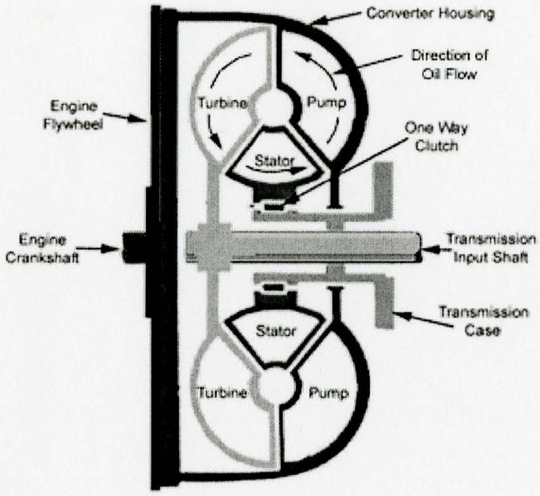

Figure 1.1. Cross section of a torque converter, by Ofria, 2000.

In automatic transmission vehicles, torque converters are used in place of mechanical coupling used in standard shift vehicles. It is there to allow the engine to continue running when the vehicle comes to a stop. A torque converter is a fluid coupling device. The principle behind its operation is similar to air flow couplings as shown in figure 1.2. Instead of air, the difference with a torque converter is that it uses oil, or automatic transmission fluid (ATF), to be more precise.

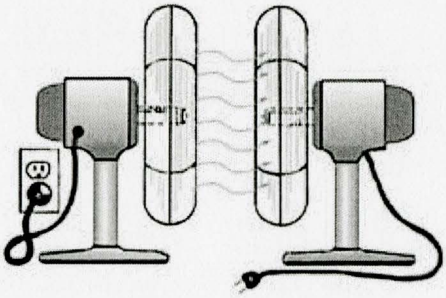

Figure 1.2. An example of air flow coupling, by Ofria, 2000.

When the engine is running, transmission fluid is pulled into the pump section and then pushed outward by centrifugal force until it reaches the turbine section and causing it to turn. The fluid continues in a circular motion back towards the center of the turbine where it enters the stator. If the turbine is moving relatively slower than the pump, the fluid will conflict with the front of the stator fins which pushes the stator into the one way clutch which prevents it from turning. With the stator stopped, the fluid is directed by the stator fins to re-enter the pump at a "helping" angle providing a torque increase. As the speed of the turbine approaches the speed of the pump, the fluid starts hitting the stator blades on the back-side causing the stator to turn in the same direction as the pump and turbine. As the speed increases, all three elements turn at approximately the same speed.

Since the 1980's, in order to improve fuel economy, torque converters have been equipped with a lockup clutch which locks the turbine to the pump as the vehicle speed reaches approximately 70 - 80 KPH. This lockup is controlled by computer and usually would not engage unless the transmission is in the third or fourth gear.

There are usually four parameters used to define the performance of torque converters:

1. Speed ratio, defined as: $SR = \frac{\Omega_t}{\Omega_p}$

Where:

Ω_t is the rotational speed of the turbine, Ω_p is the rotational speed of the pump.

2. Torque ratio, defined as: $TR = \frac{T_t}{T_p}$

Where:

T_t is the turbine torque, T_p is the pump torque.

3. Efficiency, defined as: $\eta = SR \times TR$.

4. K-factor, defined as: $K = \frac{\Omega_p}{\sqrt{T_p}}$, is the unit torque produced at a certain rpm.

1.2. Cavitation (Brennen, 1995)

Cavitation is a general term used to describe the formation of vapor bubbles in a liquid. Cavitation is usually classified into two types: inertial (or transient) cavitation and non-inertial cavitation. In inertial cavitation, a vapor bubble in a liquid rapidly collapses, producing a shock wave. Such cavitation often occurs in pumps, propellers, impellers, and in the vascular tissues of plants. Non-inertial cavitation is the process where a bubble in a fluid is forced to oscillate in size or shape due to some form of energy input, such as an acoustic field. Such cavitation is often found in ultrasonic cleaning baths, and could also be observed in pumps and propellers etc.

In many cases, cavitation is an undesirable process. In devices such as propellers and pumps, cavitation causes significant noise, mechanical damage to components, vibrations, and loss of efficiency.

When cavitation bubbles collapse, they focus the liquids energy to very small volumes. Thereby, they create regions of high velocity and temperature and produce shock waves which are the source of noise. The noise created by cavitation is a particular problem for submarines, where it aids counter detection.

Although the collapse of cavities is a relatively low energy event, it is highly localized and can even erode metals such as steel. The pitting caused by the collapse of cavities produces great wear on components and can dramatically shorten a propeller or pump's lifetime.

Although cavitation is undesirable in many circumstances, this is not always the case. For example, supercavitating torpedoes in use by the military envelop the torpedo in a large bubble of cavitation. By significantly reducing or eliminating contact with water, these torpedoes can travel considerably faster than conventional torpedoes.

Cavitation can also be a boon in ultrasonic cleaning devices. These devices effect cavitation using sound waves and use the collapse of the cavitation bubbles to clean surfaces. Used in this manner, the need for environmentally harmful chemicals can be reduced in many industrial and commercial processes that require cleaning. Still the details on how bubbles clean are not very well understood.

Major places where cavitation occurs are in pumps, on propellers, or at restrictions in a flowing liquid. As an impeller's (in a pump), or propeller's (as in the case of a ship or submarine) blades move through a fluid, low pressure areas are formed as the fluid accelerates around and moves past the blades. The faster the blades move, the lower the pressure around it can become. As pressure reaches the vapor pressure, the liquid vaporizes and forms small bubbles, which is cavitation. When the bubbles collapse later, they typically cause very strong local shockwaves in the fluid, which may be audible and may even damage the blades.

Cavitation in pumps may occur in two different forms:

1.2.1. Suction cavitation

Suction cavitation occurs when the pump suction is under a low pressure condition where the liquid turns into a vapor at the eye of the pump impeller. This vapor is carried over to the discharge side of the pump where it no longer sees vacuum and is compressed back into a liquid by the discharge pressure. This imploding action occurs violently and attacks the face of the impeller. An impeller that has been operating under a suction cavitation condition can have large pieces of material removed from its face causing premature failure of the pump.

1.2.2. Discharge cavitation

Discharge cavitation occurs when the pump discharge pressure is extremely high, normally occurring in a pump that is running at less than 10% of its best efficiency point. The high discharge pressure causes the majority of the fluid to circulate inside the pump instead of being allowed to flow out the discharge. As the liquid flows around the impeller it must pass through the small clearance between the impeller and the pump cutwater at extremely high velocity. This velocity causes a vacuum to develop at the cutwater (similar to what occurs in a venturi) which turns the liquid into a vapor. A pump that has been operating under these conditions shows premature wear of the impeller vane tips and the pump cutwater. In addition, due to the high pressure conditions, premature failure of the pump's mechanical seal and bearings can be expected. Under extreme conditions, this can break the impeller shaft.

1.3 Turbulence (Davidson, 2003)

Most of the flow which we experience in daily life is turbulent. Typical examples are flow around cars, planes and lighted cigarettes. Also the combustion flow in engines, both in piston engines and gas turbines and combustors, are highly turbulent. Air movements in rooms are also turbulent. Especially, the flow and cavitation inside torque converters is turbulent. In turbulent flow we usually divide the variables in one time-averaged part, $\overline{U}$, which is independent of time (when the mean flow is steady), and one fluctuating part u so that $U = \overline{U} + u$.

There is not a clear definition of turbulent flow, but it has a number of characteristic features (see Tennekes et al. 1972) such as:

i. Irregularity

Turbulent flow is random, irregular and chaotic. The flow consists of a series of different eddy sizes (scales) where largest eddies are of the order of the flow geometry (i.e. boundary layer thickness, jet diameter, etc). On the other hand we have the smallest eddies which are by viscous forces or stresses dissipated into internal energy. Even though turbulence is chaotic it is deterministic and can be described by the Navier-Stokes equations.

ii. Diffusivity

The diffusivity increases in turbulent flow, which means that the spreading rate of boundary layers, jets, etc. increases as the flow becomes turbulent. The turbulence increases the exchange rate of momentum in e.g. boundary layers and reduces or delays further separation at bluff bodies such as cylinders, and vehicles. The increased diffusivity also increases the wall friction in internal flows such as in ducts and pipes.

iii. High Reynolds numbers

Turbulent flow occurs at high Reynolds number. For example, the transition to turbulent flow in pipes occurs at $\mathrm{Re}_D \simeq 2300$ and in boundary layers at $\mathrm{Re}_x \simeq 100000$.

iv. Three-dimensional

Turbulence is three-dimensional. However, when the equations are time averaged it can be treated as two-dimensional flow.

v. Dissipation

Turbulent flow is highly dissipative, which means that kinetic energy in the small eddies are transformed into internal energy. The small eddies receive the kinetic energy from larger eddies. The larger eddies receive their energy from even larger eddies and so on. The largest eddies extract their energy from the mean flow. This process of transferred energy from the largest turbulent eddies to the smallest is called cascade process.

vi. Continuum

Even though we have small turbulent scales in the flow they are much larger than the molecular scale and we can treat turbulent flow as a continuum.

1.4 Research on flow inside torque converters

Improving torque converter performance depends heavily on developing improved computational flow modeling and design methods. Many investigations have been carried out on fluid flow inside torque converters, some of which are described below. The literature review is divided into three subsections: introduction, experimental research, and computational research.

1.4.1 Introduction

In a torque converter, automatic transmission fluid (ATF) is in a continuous closed-loop flow through pump, turbine, and stator. At the local temperature, if local pressure at one place drops under vapor pressure, vapor cavities will occur at that place. Similarly, at one fixed local pressure, if the temperature at one place increases over the saturation temperature corresponding to the fluid vapor pressure at that point, vapor cavities will typically form at that place.

In many cases, there will always be cavitation nuclei in the form of undissolved and dissolved gases together with solid particles in the liquid. These can cause cavitation in actual liquids to start at pressures higher than the vapor pressure, which means that cavitation may start even before local absolute pressure drops below local vapor pressure. In torque converters, the lowest absolute pressure region is expected to occur in the suction side of stator blades. The low local absolute pressure region may occur due to Bernoulli Effect, i.e. due to flow velocity increase through the stator passage. It also may occur due to laminar boundary layer separation that occurs at stator entrance according to different inlet flow angles at stator leading edge. This analysis resembles the analysis of cavitation over a hydrofoil due to different angles of attack studied by Yves Lecoffre (1999). Thus the suction side of the stator blade is expected to be the most appropriate region for the formation of vapor bubbles.

After vapor bubbles are entrained in the flow of ATF, they will suddenly collapse as the ATF passes through a region where the absolute pressure, along the flow path, rises above vapor pressure, which occurs as the ATF flows from the stator to the pump where absolute pressure is increased. Moreover, although the suction side is the region of the lowest pressure, there still exist some places on the pressure side of the stator where the absolute pressure is likely to be higher than the vapor pressure. Therefore, collapse of vapor bubbles could take place anywhere in the zone connecting the high pressure regions of the stator to the high pressure regions at the pump exit.

There is a need now to make torque converters axially shorter but still achieve good performance and efficiency. Small size torque converters have advantages in weight and space saving, but are undesirable for cavitation, capacity, torque ratio, and efficiency, as studied by Dong et al. (2002).

Cavitation can be suppressed by increasing the supply pressure of transmission's hydraulic control system. Increasing charge pressure to raise the torque at which cavitation might occur. Maximum charge pressure is limited by the pressure vessel characteristics of the torque converter and by the capacity of the transmission pump.

1.4.2 Experimental research

Experimental research identified main features of flow in hydraulic torque converters. Measurement techniques include laser velocimetry, and fast response five-hole probe (A equipment that precisely measures the fluid velocity). Laser Doppler Velocimetry (LDV) is the measurement of fluid velocities by detecting shift in Doppler frequency of laser light that has been scattered by small particles moving with the fluid. Using this technique, velocities were measured at various locations inside torque converters. Brun et al. (1996) and Brun and Flack (1997) carried out experimental studies using a torque converter at University of Virginia. Work was done on torque converters with various blade and torus shapes and at various speed ratios. The measurements were done at various locations inside pump, turbine, and stator.

Marathe et al. (1997) used a five-hole probe to measure the flow at the exit of the stator at different operating conditions. Dongan et al. (1998) used a high-frequency-response five-hole probe to measure steady and unsteady flow fields at pump and turbine exits of a 245mm GM torque converter. This work was done at the Penn State University.

Von Backstorm et al. (1996) provided a thorough review of the experimental results of the work carried out by the Penn State group and by the University of Virginia group. They also provided an assessment of fluid flow inside automotive torque converters. Main features of flow in the pump, turbine and stator were discussed. In both pump and turbine, the through flow velocity is high near the pressure surface shell corner while the flow near the suction surface core is highly turbulent and may be separated and reversed. The position of the stator in a passage curved in the meridional plane leads to secondary flow and low velocities at the core near the pump inlet. Velocity gradients coupled with flow turning and rotation led to strong secondary flows in pump and turbine passages.

Anderson et al. (2003) investigated cavitation signatures in an automotive torque converter under stall conditions experimentally. A criterion was proposed for predicting early and advanced cavitation in terms of non-dimensional pump speed. The dimensionless pump speed that marks early cavitation is obtained by relating this parameter to appearance of charge-pressure dependent pressure (see figure 1.3) fluctuations in the differential pressure transducer readings. The data were transmitted from the differential pressure transducers by a wireless telemetry system mounted on the pump housing. Data were received and processed by a data acquisition system.

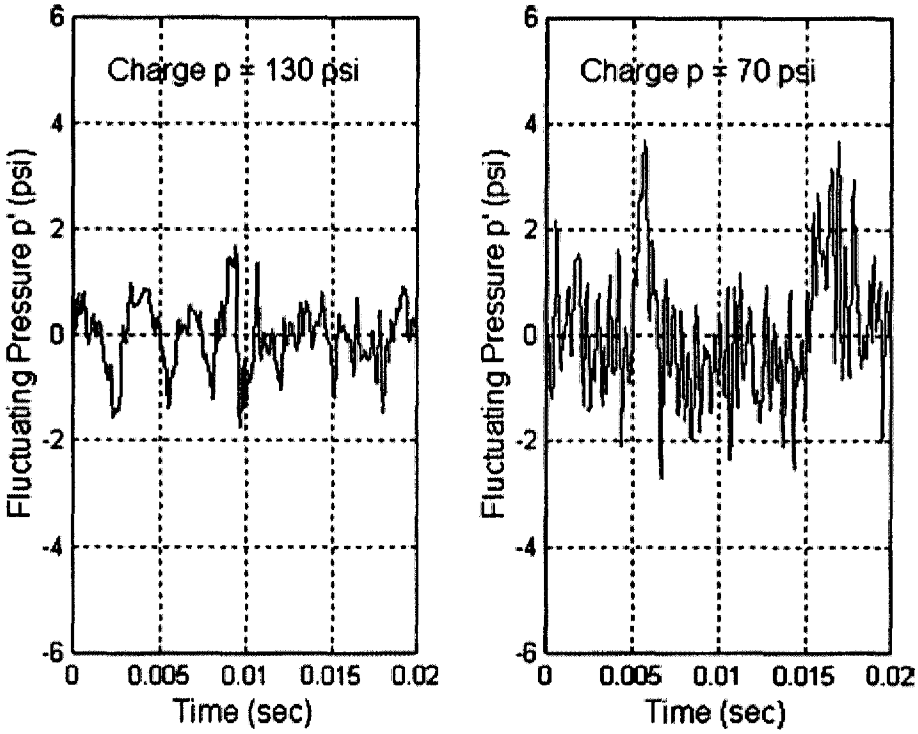

Figure 1.3. Pressure fluctuations at two charge pressures reported by Anderson et al. (2003).

ATF exhibited cavitation for charge pressures in the range of 70-130 psi and pump speeds in the range of 2000-2500 rpm (see figure 1.4). In figure 1.4, as the rotational speed increased over 2000 rpm, the pump torque curves started to diverge from the ideal curve, which is a strong indication of the cavitation existence. Increasing the pump speed has smaller impacts on the pump torque curves obtained at higher charge pressures. For different torque-converter designs and a given transmission fluid, their proposed non-dimensional pump-speed criteria was capable of marking early and advanced stages of cavitation for a range of torque-converter sizes and a range of charge pressures.

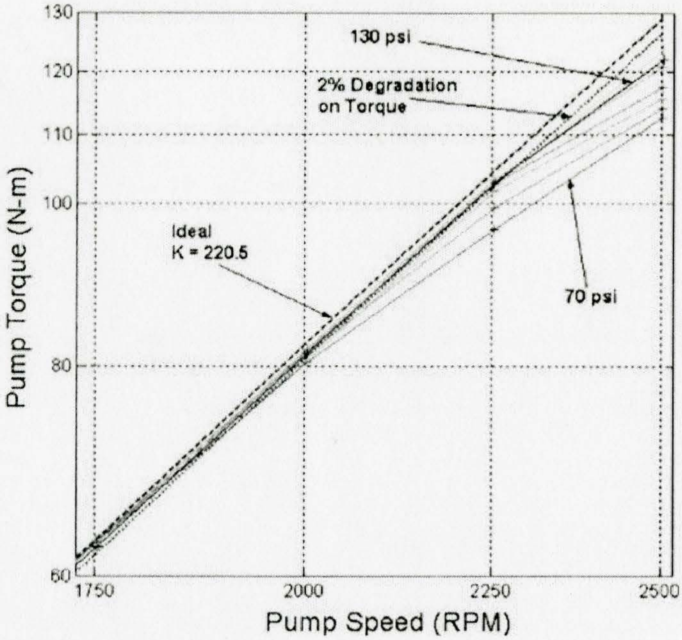

Figure 1.4. The pump torque measured between 70 psi to 130 psi at pump speed between 1750 rmp to 2500 rpm, as reported by Anderson et al. (2003).

Mekkes et al. (2004) measured static pressure on the nose of a torque converter stator blade. They concluded that the attached cavitation does not form on the stator blade nose.

1.4.3 Numerical research

Computational Fluid Dynamics (CFD) is very helpful in analyzing and understanding flow behavior in complex flow situations such as flows in torque converters. With the rapid progress in computer technology, it is possible to compute complicated three-dimensional flow field inside a torque converter. Traditionally, experiments were used in design and development of new torque converters. An exact model of a torque converter, which is machined from solid turbines, pumps and stators, would be obtained to test several torque converter combinations. A single machining of a solid torque converter assembly can take six months to produce and cost around $50,000, as reported by Schweitzer et al. (2003). The use of CFD allows the investigation of more design iterations in less time and with less cost than traditional methods.

1.4.3.1 Numerical research on the flow inside torque converters

Computational work in torque converters started from the work done by Abe et al. (1991). They simulated internal flow field inside a torque converter using a steady-interaction technique and a third-order upwind scheme. They confirmed that flow is three-dimensional. Bai et al. (1997) solved Navier-Stokes equations for fluid couplings. Schulz et al. (1996) described a numerical method for calculating three-dimensional, steady and unsteady, incompressible, viscous flow to calculate internal flow fields in torque converters. The calculations showed uniform flow conditions at stator outlet for a wide operating range. They showed also that unsteady interaction of stator with pump or turbine is negligible. By et al. (1995) modified a Navier-Stokes code for torque converter flow field computations and computed the secondary flow patterns in pump of an automotive torque converter. With the appearance of commercial CFD software, more and more researchers have started using these codes for performance as well as design purposes.

Shin et al. (2000) investigated the effect of scroll angle of pump and turbine blades on the performance of torque converters. The internal flow field of an automotive torque converter was calculated using the 3-D Navier-Stokes flow code with a mixing plane. Schweitzer et al. (2003) presented some of the computational fluid dynamics work done on a three-element torque converter using a commercially available package CFX-TASCFLOW. Good qualitative agreement was found between the computational results and available experimental velocity data, which validated the computational results.

Lee et al. (2000) described a simulation procedure to calculate torque converter performance parameters. Unstructured grid and steady state algorithm in the rotating reference frame were used. A real computation was performed using the commercial CFD package, Fluent/UNS 4.2. The maximum error in predicted torque ratio and capacity factor was less than 15%. Dong et al. (2002) used CFD simulation to develop new stators for stall torque ratio and K-factor ($K = \frac{\Omega_p}{\sqrt{T_p}}$) improvement. They simulated flow fields of both baseline and new (modified) torque converters. The overall performance of each converter was calculated from flow data and correlated with dynamometer test results. Torque capacity of the new converter largely increased without decreasing peak efficiency under all operation conditions. They also investigated the effects of core leakage flow and sealing gap. The core region was modeled and coupled together with other three major components of torque converter. Results showed that core leakage flow could result in a 3.6% reduction of stall torque ratio and 2% decrease in peak efficiency.

Cavitation is thought to form in the free-shear layer in the flow separation zone, see Fig.1.5. The minimum pressure measured did not drop to the saturation pressure of ATF. As a result attached cavitation near the nose of the stator blade was ruled out. The drop in pressure on the pressure side of the blade with increasing pump speed did not agree with CFD predictions reported by Mekkes et al. (2004).

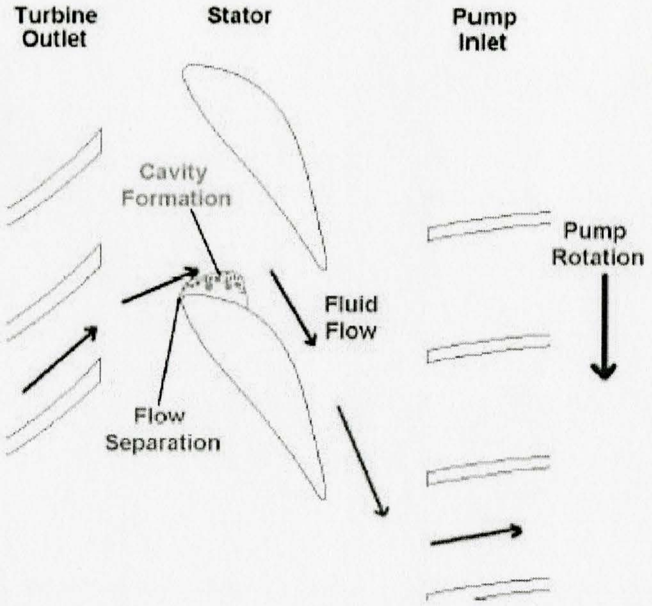

Figure 1.5. Schematic of expected region of cavitation formation, Mekkes et al. (2004)

Dong et al. (2002) used CFD simulation to predict torque converter performance at different input torques using a constant enthalpy vaporization model. They concluded that the variation of input torque observed in dynamometer tests is due to the cavitation in the torque converter. Cavitation occurred at high input torque and low speed ratio conditions because of the high volume flow rate and large incidence angle at the stator inlet. Because of the unsteady nature of the cavitation flow, their results are considered as time averaged values. The process of vapor bubble growing and collapsing is not shown in their results. The K-factor curves for different input torque levels are shown in figure 1.6. Results show that torque capacity decreases with increased input torque due to cavitation. Cavitation occurred only at low speed ratio conditions (below 0.4). Dong et al. studied cavitation at stall condition only because it is the worst condition. They also studied cavitation at fixed charge pressures.

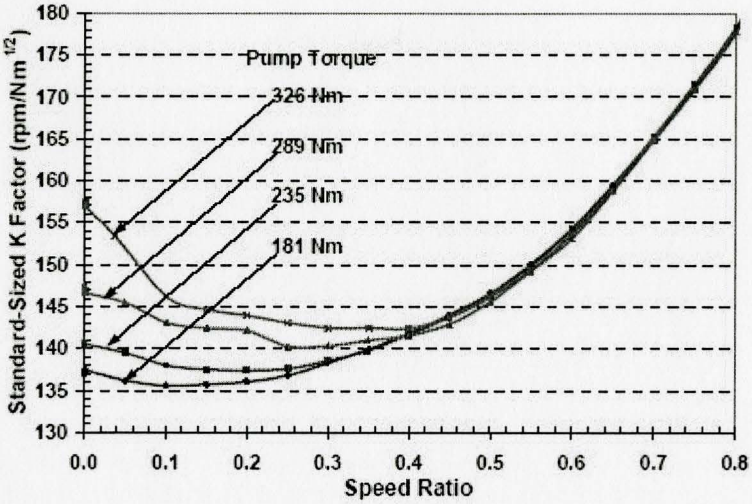

Figure 1.6. K-factor vs. speed ratio for different input torque (Dynamometer Test), Dong et al. (2002).

1.4.3.2 Cavitation modeling

Cavitation modeling has been improved in the last few years. Recent studies coupled the solution of Navier-Stokes equation with a cavitation model. These models are known as two-phase flow models also known as homogenous equilibrium flow models. Difference between models comes from the relation that defines density of the field. These models can treat traveling as well as attached cavitation (Chen et al., 1995). Different researchers used a barotropic approach (Delgosha, 2002). In this approach, fluid density ρ varies in the computational domain according to a barotropic state law $\rho = \rho(P)$ that links density to local static pressure. While this approach gives some good results, it seems to be oversimplified since density in cavitation flows must be related not simply to local pressure, but to the time-dependant bubble evolution caused by changes in the pressure field.

Singhal et al. (2002) developed a cavitation model considering the following first-order effects:

- Formation and transport of vapour bubbles.

- Turbulent fluctuations of pressure and velocity.

- Magnitude of non-condensable gases, which are dissolved or ingested in the operating liquid.

The phase change rate expressions are derived from a reduced form of Rayleigh-Plesset equation for bubble dynamics (without viscosity and surface tension effects). These rates depend on local flow conditions (pressure, velocities and turbulence) as well as on fluid properties (saturation pressure, densities, and surface tension). The rate expressions employ two empirical constants, which have been calibrated with experimental data to cover different flow conditions.

Zwart et al. (2004) developed a cavitation model to be implemented in a finite volume method. The model is based on multi-phase flow equations, with mass transfer due to cavitation appearing as a source term in the liquid and vapor continuity equations. The mass transfer rate is derived from a simplified Rayleigh-Plesset equation which neglects the effect of viscosity, surface tension, and gas inside the bubble. This model was utilized by ANSYS-CFX10.0/11.0.

Zwart et al. (2004) validated their model by applying it to the following three cases and compared the numerical results with experimental data.

1- Venturi cavitation (Figure 1.7.)

2- Hydrofoil cavitation (Figure 1.8.)

3- Inducer cavitation (Figure 1.9.)

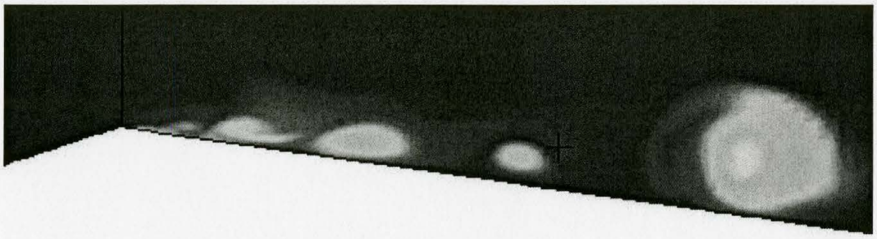

Figure 1.7. Snapshot of volume fraction in a venturi, as reported by Zwart et al. (2004).

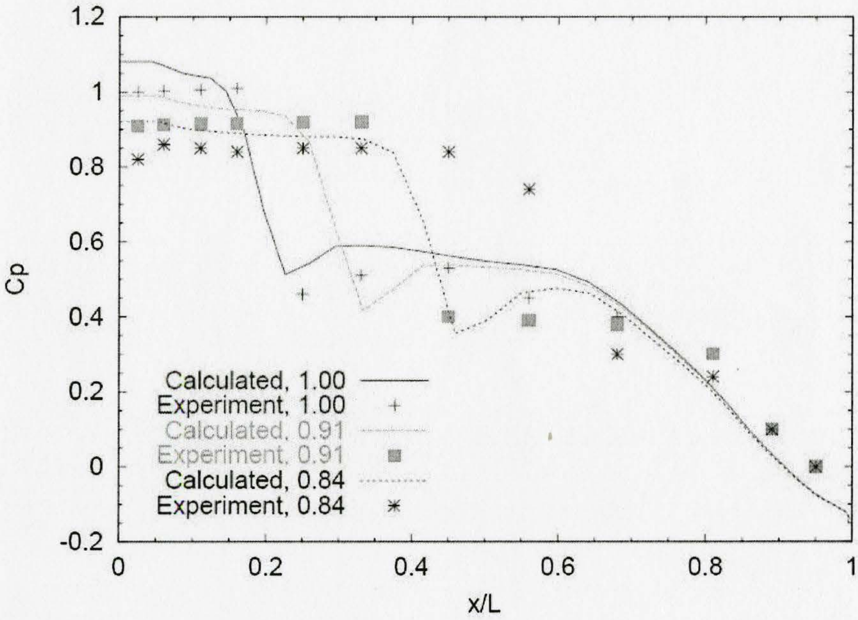

Figure 1.8. Comparison of experimental and computed surface pressure coefficients for leading edge cavitation on hydrofoil at three cavitation numbers, as reported by Zwart et al. (2004).

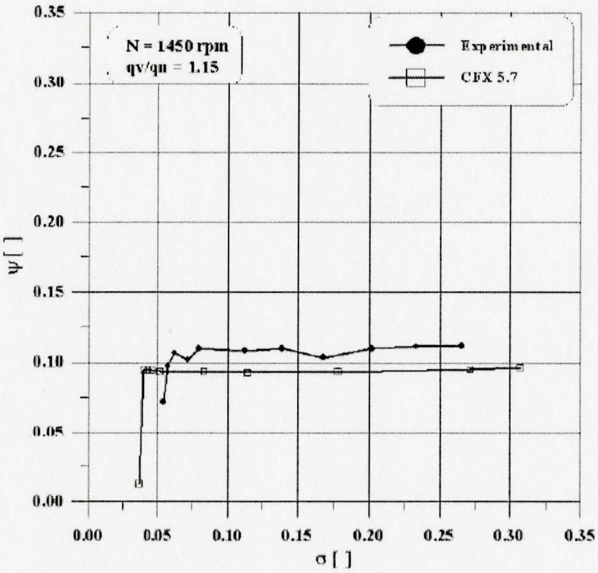

Figure 1.9. Predicted and experimental head drop against cavitation number for cavitation inside flow inducer, as reported by Zwart et al. (2004).

It is worth mentioning here that Zwart et al. (2004) had to change the values of the model empirical coefficients for the case of cavitation inside a venturi. Results shown in figure 1.7. have been obtained by changing the value of the vaporization coefficient from the default value of 50 to 0.4 and that of the condensation coefficient from the default value of 0.01 to 0.001.

It is also worth noting here that using this model in solving a new cavitation problem without knowing the right values of the two empirical coefficients a priori is regarded as a big disadvantage of this model.

1.4.3.3 Effect of viscosity and surface tension on bubble growth and collapse

Poritsky (1951) examined the effects of viscosity on the motion of a spherical bubble with constant internal pressure. Poritsky's treatment modified the Rayleigh analysis resulting in the following second-order differential equation for bubble wall motion described by Brennen (1995):

$$R\ddot{R}+\frac{3}{2}\left(\dot{R}\right)^2=\frac{P_v-P_\infty}{\rho_L}+\frac{P_{Go}}{\rho_L}\left(\frac{R_o}{R}\right)^{3k}-\frac{4\mu_L\dot{R}}{\rho_L R}-\frac{2\sigma_L}{\rho_L R} \tag{1.1}$$

where:

R is the bubble radius,

σ_L is the surface tension of the liquid,

P_v is the saturated vapour pressure,

P_∞ is the pressure of the liquid surrounding the bubble,

ρ and μ are physical properties of the liquid.

Poritsky (1951) found that the rate of growth and collapse is strongly affected by both viscosity and surface tension, as shown in figures 1.10 and 1.11. In case of collapse, Fig. 1.10, Poritsky defined the following parameters:

for $P_\infty > P_v$, bubble collapse

$$C=\mu'=\frac{4\mu}{R_o\sqrt{\rho(P_\infty-P_v)}} \tag{1.2}$$

$$D=\sigma'=\frac{\sigma}{R_o\sqrt{\rho(P_\infty-P_v)}} \tag{1.3}$$

and dimensionless time $\frac{R}{R_o}$ (1.4)

for $P_\infty < P_v$, bubble growth

$$C=\mu'=\frac{4\mu}{R_o\sqrt{\rho(P_v-P_\infty)}} \tag{1.5}$$

$$D=\sigma'=\frac{\sigma}{R_o\sqrt{\rho(P_v-P_\infty)}} \tag{1.6}$$

and dimensionless time $\frac{t}{R_o}\sqrt{\frac{P_v - P_\infty}{\rho}}$ (1.7)

Dimensionless radius in both cases is defined as: $\frac{R}{R_o}$ (1.8)

Figures 1.10 and 1.11 indicate that fluid viscosity tends to decrease both the growth rate and collapse rate, whereas surface tension tends to decrease growth rate but increase collapse rate. During growth, surface tension decreases the expansion rate in the early stages but not in the late stages. Similarly, the latter stages of collapse show the greatest effect of surface tension.

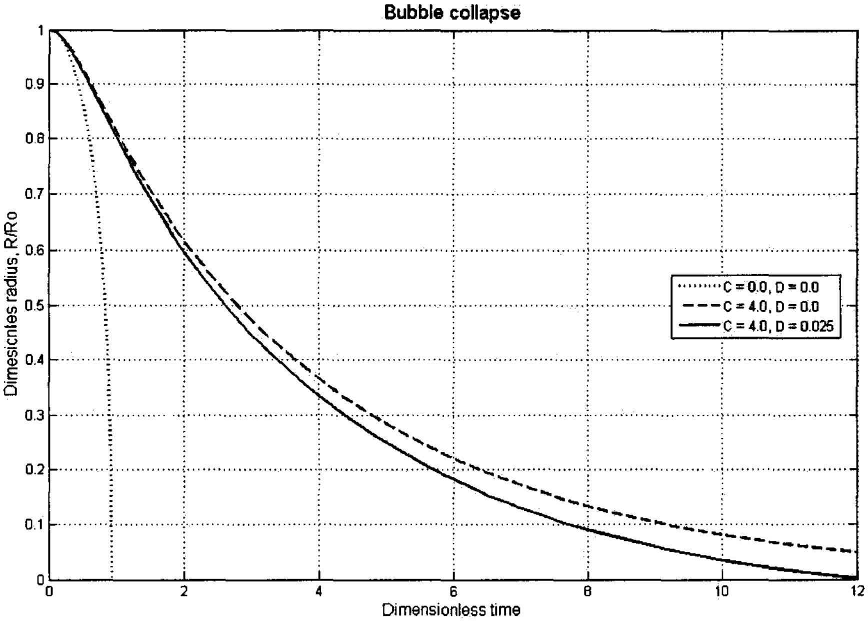

Figure 1.10. Collapse of a spherical bubble in an incompressible liquid with and without surface tension, adapted from Poritsky (1951).

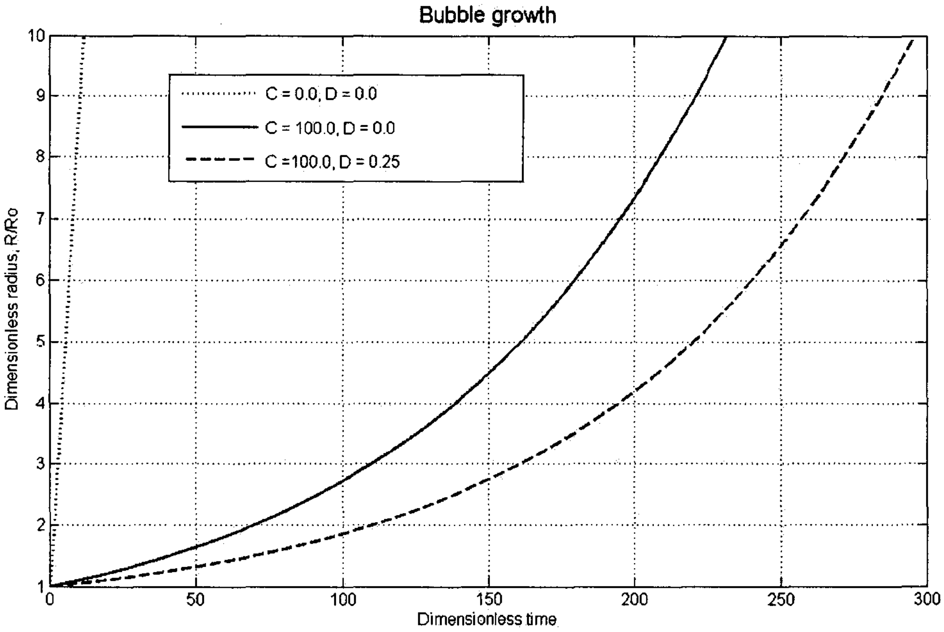

Figure 1.11. Growth of a spherical bubble in an incompressible liquid with and without viscosity and surface tension, adapted from Poritsky (1951).

Shu (1951) demonstrated that Proitsky's equation (1.1) for the bubble motion without surface tension leads to an infinite collapsing time if the dimensionless parameter

$$C = \mu' = \frac{4\mu}{R_o\sqrt{\rho\left(P_\infty - P_v\right)}} \tag{1.2}$$

exceeds a certain critical value. Poritsky (1951) found the critical value of $\mu'$to be 0.46. Shu (1951) analytically proved the existence of such critical value. That is, bubble motion without the effect of surface tension has an infinite collapsing time if $\mu' \geq 0.46$.

Ivany (1965) discussed the effect of viscosity and its relation to the boundary condition at the bubble wall. The effect of viscosity is to increase liquid pressure at the bubble wall during collapse. The bubble wall velocity in the incompressible analysis decreased as viscosity increased, see Fig. 1.12. The effect of viscosity at low viscosity values (e.g. for cold water) becomes significant only for radius ratios of 10^{-3} to 10^{-4}. For a viscosity of approximately 100 times that of coldwater, the effect of viscosity becomes significant for radius ratios in the range 10^{-2} to 10^{-3}. Therefore, the effect of viscosity can be only substantial for liquids with viscosities in the range of those of lubricating oils in Hammitt (1980).

Hammitt (1980) summarized different studies on the effect of viscosity on bubble collapse. Results in Hammitt (1980) confirmed that the effect of viscosity can only be substantial for liquids with viscosity in the range of lubricating oils.

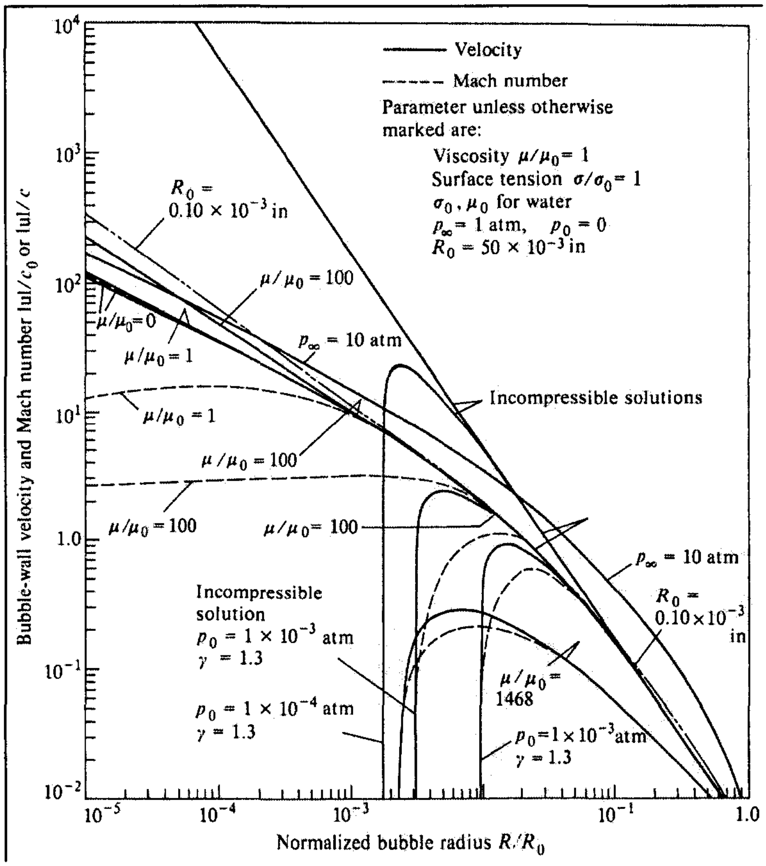

Figure 1.12. Bubble-wall velocity and Mach number vs. normalized bubble radius for reference

bubble parameters except where noted otherwise on individual curves reported by Ivany (1965).

1.5 Research objectives and scope of work

1.5.1 Introduction

From a literature review of previous work, it was found that a large number of studies to investigate the cavitation phenomenon inside automotive torque converters have been carried out and a good understanding of experimental and computational work has been established. However, as per the best knowledge of the author, there are still some blind spots:

Most of the previous studies have not used the only implemented cavitation model developed by Zwart et al. (2004) in ANSYS-CFX10.0/11.0. It has been suggested by Zwart et al. (2004) that modifications need to be applied to the cavitation model in some cases. Hence, there is a need for determining the effects of three empirical parameters (condensation coefficient, vaporization coefficient, and vapor pressure.) in the new cavitation model and an efficient procedure of using CFX10.0/11.0 to predict cavitation.

Very limited turbulence models were used in previous studies. Hence, there is a need to investigate the effect of using different turbulence models in cavitation prediction.

Most of the previous studies were limited to steady state simulations. Due to the unsteady nature of cavitation, there is a significant need to study cavitation using transient state simulations.

GM, the sponsor of this project, showed great interest in simulating complex flow and cavitation inside torque converters. According to experimental results obtained by GM Powertrain, significant effect of cavitation in a dynamometer test cell has been observed and cavitation is believed to contribute to unacceptable performance variation, noise, and damage to the blades. Cavitation happens when the level of input torque applied to torque converter pump increases which result in dropping the pressure on the suction side of the stator blades below the vapor pressure of the fluid, allowing the fluid to evaporate. Cavitation causes powertrain noise and reduces fuel economy. It also decreases torque capacity of torque converter. Existence of cavitation is higher due to temperature in hot summer days and reduction of torque converter size. Hence, study of cavitation is important to understand design and operation conditions used to maintain good torque converter performance and control noise.

1.5.2 Objectives of the present study

1. To simulate flow and cavitation inside torque converters by using the current cavitation model built in ANSYS CFX10.0/11.0.
2. To investigate the effect of vapor pressure.
3. To investigate the effect of using different turbulence models.
4. To examine the difference between numerical results obtained using steady and transient simulations.

Chapter 2 Mathematical Formulation

2.1 Governing equations (Davidson, 2003)

When the flow is turbulent it is preferable to decompose the instantaneous variables (i.e. velocity components and pressure) into a mean value and a fluctuating value, i.e.

$$U_i = \overline{U}_i + u_i$$

$$P = \overline{P} + p \tag{2.1}$$

One reason to decompose the variables is that when measuring flow quantities people are usually interested in the mean values rather that the time histories. Another reason is that when solving the Navier-Stokes equation numerically it would require a very fine grid to resolve all turbulent scales and it would also require a fine resolution in time (turbulent flow is always unsteady).

The continuity equation and the Navier-Stokes equation read:

$$\frac{\partial \rho}{\partial t} + \left(\rho U_i\right)_{,i} = 0 \tag{2.2}$$

$$\frac{\partial \rho U_i}{\partial t} + \left(\rho U_i U_j\right)_{,j} = -P_{,i} + \left[\mu\left(U_{i,j} + U_{j,i} - \frac{2}{3}\delta_{ij}U_{k,k}\right)\right]_{,j} \tag{2.3}$$

Where $(.)_{,j}$ denotes derivation with respect to x_j. With the assumption of the flow is incompressible (i.e. low Mach number) the dilatation term on the right hand side of Eq. 2.3 is neglected so that:

$$\frac{\partial \rho U_i}{\partial t}+\left(\rho U_i U_j\right)_{,j}=-P_{,i}+\left[\mu\left(U_{i,j}+U_{j,i}\right)\right]_{,j} \tag{2.4}$$

It is important to note that the term "incompressible" in the sense that density is independent of pressure ($\partial P / \partial \rho = 0$), but it does not mean that density is constant; it can be dependent on for example temperature or concentration.

Substituting Eq. 2.1 into the continuity equation (2.2) and the Navier-Stokes equation (2.4) we obtain the time averaged continuity equation and Navier-Stokes equation:

$$\frac{\partial \rho}{\partial t}+\left(\rho \overline{U}_i\right)_{,i}=0 \tag{2.5}$$

$$\frac{\partial \rho \overline{U}_i}{\partial t}+\left(\rho \overline{U}_i \overline{U}_j\right)_{,j}=-\overline{P}_{,i}+\left[\mu\left(\overline{U}_{i,j}+\overline{U}_{j,i}\right)-\rho \overline{u_i u_j}\right]_{,j} \tag{2.6}$$

A new term $\overline{u_i u_j}$ appears on the right-hand side of Eq. 2.6 which is called the Reynolds stress tensor. The tensor is symmetric (i.e. $\overline{u_1 u_2}=\overline{u_2 u_1}$). It represents correlations between fluctuating velocities. It is an additional stress term due to turbulence (fluctuating velocities) and it is unknown. A model for $\overline{u_i u_j}$ is needed to close the equation system in Eq. 2.6.

This is called the closure problem: the number of unknowns (ten: three velocity components, pressure, six stresses) is larger than the number of equations (four: the continuity equation and three components of the Navier-Stokes equations).

Hence further equations and correlations are needed to solve the problem.

Boussinesq assumption

In eddy viscosity turbulence models the Reynolds stresses are linked to the velocity gradients via the turbulent viscosity: this relation is called the Boussinesq assumption, where the Reynolds stress tensor in the time averaged Navier-Stokes equation is replaced by the turbulent viscosity multiplied by the velocity gradients. To show this we introduce this assumption for the diffusion term at the right-hand side of Eq. 2.6:

$$\left[\mu\left(\overline{U}_{i,j}+\overline{U}_{j,i}\right)-\rho\overline{u_i u_j}\right]_{,j}=\left[(\mu+\mu_t)\left(\overline{U}_{i,j}+\overline{U}_{j,i}\right)\right]_{,j}$$

which gives:

$$\rho\overline{u_i u_j}=-\mu_t\left(\overline{U}_{i,j}+\overline{U}_{j,i}\right) \tag{2.7}$$

If we in Eq. 2.7 do a contraction (i.e. setting $i=j$) the right-hand side gives:

$$\overline{u_i u_j}\equiv 2k$$

where k is the turbulent kinetic energy. On the other hand the continuity equation (Eq. 2.5) gives that the right-hand side of Eq. 2.7 is equal to zero. In order to make Eq. 2.7 valid upon contraction we add $2/3\rho\delta_{ij}k$ to the left-hand side of Eq. 2.7 so that:

$$\rho\overline{u_i u_j}=-\mu_t\left(\overline{U}_{i,j}+\overline{U}_{j,i}\right)+\frac{2}{3}\rho\delta_{ij}k \tag{2.8}$$

Note that contraction of δ_{ij} gives:

$$\delta_{ii}=\delta_{11}+\delta_{22}+\delta_{33}=1+1+1=3$$

2.2 Turbulence closure models

2.2.1 Standard k-ε turbulence model

The standard k-ε model is a semi-empirical model based on modeling the turbulent kinetic energy *k*, and its dissipation rate ε. In the derivation of the k-ε model, it is assumed that the flow is fully turbulent, and the effects of molecular viscosity are negligible. Therefore, the standard k-ε model is only valid for fully turbulent flows.

Transport equations for the standard k-ε model

The turbulent kinetic energy, *k*, and its rate of dissipation, ε, are obtained from the following transport equations:

$$\frac{\partial(\rho k)}{\partial t}+\frac{\partial(\rho U_j k)}{\partial x_j}=P_k-\rho\varepsilon+\frac{\partial}{\partial x_j}\left(\Gamma_k\frac{\partial k}{\partial x_j}\right) \tag{2.9}$$

and

$$\frac{\partial(\rho\varepsilon)}{\partial t}+\frac{\partial(\rho U_j\varepsilon)}{\partial x_j}=C_{\varepsilon 1}\frac{\varepsilon}{k}P_k-C_{\varepsilon 2}\rho\frac{\varepsilon^2}{k}+\frac{\partial}{\partial x_j}\left(\Gamma_\varepsilon\frac{\partial\varepsilon}{\partial x_j}\right) \tag{2.10}$$

with

$$\Gamma_k=\mu+\frac{\mu_t}{\sigma_k}$$

$$\Gamma_\varepsilon=\mu+\frac{\mu_t}{\sigma_\varepsilon} \tag{2.11}$$

In these equations, P_k represents the generation of turbulent kinetic energy due to the mean velocity gradients:

$$P_k=\mu_t\left(\frac{\partial U_i}{\partial U_j}+\frac{\partial U_j}{\partial x_j}\right)\frac{\partial U_j}{\partial x_j}+\frac{2}{3}\rho k\delta_{ij}\frac{\partial U_i}{\partial x_j}$$

$C_{\varepsilon 1}$, $C_{\varepsilon 2}$, σ_k and σ_ε are constants.

Modeling the turbulent viscosity

The "eddy" or turbulent viscosity, μ_t, is computed by combining k and ε as follows:

$$u_\tau = \left[\left(u_\tau^{Vis}\right)^4 + \left(u_\tau^{\log}\right)^4 \right]^{0.25} \quad \mu_t = C_\mu \rho \frac{k^2}{\varepsilon} \tag{2.12}$$

where C_μ is a constant. The turbulent stresses are computed from:

$$\rho \overline{U_i U_j} = -\mu \left(\frac{\partial U_i}{\partial x_j} + \frac{\partial U_j}{\partial x_i} \right) + \frac{2}{3} \rho k \delta_{ij}$$

Model constants

The model constants $C_{\varepsilon 1}$, $C_{\varepsilon 2}$, C_μ, σ_k and σ_ε have the following default values:

$C_{\varepsilon 1} = 1.44$, $C_{\varepsilon 2} = 1.92$, $C_\mu = 0.09$, $\sigma_k = 1.0$, $\sigma_\varepsilon = 1.3$

These default values have been determined from experiments for decaying turbulence, turbulent shear flows and computer optimization. They have been found to work well for a wide range of wall-bounded and free shear flows.

2.2.2 k-ω turbulence model (Wilcox, 1988, 1993)

The turbulent kinetic energy, k, and its specific dissipation rate, ω, are obtained from the following transport equations:

$$\frac{\partial(\rho k)}{\partial t} + \frac{\partial(\rho U_j k)}{\partial x_j} = P_k - \beta' \rho k \omega + \frac{\partial}{\partial x_j} \left(\Gamma_k \frac{\partial k}{\partial x_j} \right) \tag{2.13}$$

and

$$\frac{\partial(\rho \omega)}{\partial t} + \frac{\partial(\rho U_j \omega)}{\partial x_j} = \alpha \frac{\omega}{k} P_k - \beta \rho k \omega^2 + \frac{\partial}{\partial x_j} \left(\Gamma_\omega \frac{\partial \omega}{\partial x_j} \right) \tag{2.14}$$

with

$$\Gamma_k = \mu + \frac{\mu_t}{\sigma_k}, \qquad \Gamma_\omega = \mu + \frac{\mu_t}{\sigma_\omega} \tag{2.15}$$

Modeling the turbulent viscosity

The "eddy" or turbulent viscosity, μ_t, is computed by combining k and ω as follows:

$$\mu_t = \rho \frac{k}{\omega} \tag{2.16}$$

Model constants

The model constants β', α, β, σk and $\sigma\omega$ have the following default values: $\beta' = 0.09$, $\alpha = 5/9$, $\beta = 3/40$, $\sigma k = 2.0$, $\sigma\omega = 2.0$

2.2.3 Spalart-Allmaras turbulence model (Spalart and Allmaras, 1994)

The Spalart-Allmaras model is a relatively simple one-equation model that solves a modeled transport equation for the kinematic eddy viscosity. This embodies a relatively new class of one-equation model in which it is not necessary to calculate a length scale related to the local shear layer thickness. The Spalart-Allmaras model was designed specifically for aerospace applications involving wall-bounded flows and has been shown to give good results for boundary layers subjected to adverse pressure gradients. It is also gaining popularity for turbo machinery applications.

In its original form, the Spalart-Allmaras model is effectively a low-Reynolds-number model, requiring the viscous-affected region of the boundary layer to be properly resolved. In ANSYS CFX, however, the Spalart-Allmaras model has been implemented to use wall functions when the mesh resolution is not sufficiently fine. This might make it the best choice for relatively coarse simulations on coarse meshes where accurate turbulent flow computations are not critical.

Furthermore, the near-wall gradients of the transported variable in the model are much smaller than the gradients of the transported variables in the k-ω models. This might make the model less sensitive to numerical error when non-layered meshes are used inside the viscous region.

It is worth mention here, however, the Spalart-Allmaras model is still relatively new, and yet no claim is made regarding its suitability to all types of complex engineering flows. For instance, it is not reliable to predict the decay of homogeneous, isotropic turbulence. Moreover, one-equation models are often criticized for their inability to rapidly accommodate changes in length scale, which may be necessary when the flow changes suddenly from a wall-bounded to a free shear flow.

Transport equation for the Spalart-Allmaras model

The transported variable in the Spalart-Allmaras model $\tilde{\nu}$ is identical to the turbulent kinematic viscosity except in the near-wall (viscous-affected) region. The transport equation for $\tilde{\nu}$ is

$$\rho\frac{D\tilde{\nu}}{Dt}=G_v+\frac{1}{\sigma_{\tilde{\nu}}}\left[\frac{\partial}{\partial x_j}\left\{\left(\mu+\rho\tilde{\nu}\right)\frac{\partial\tilde{\nu}}{\partial x_j}\right\}+C_{b2}\rho\left(\frac{\partial\tilde{\nu}}{\partial x_j}\right)^2\right]-Y_v \qquad (2.17)$$

where G_v is the production of turbulent viscosity and Y_v is the destruction of turbulent viscosity that occurs in the near-wall region due to wall blocking and viscous damping. $\sigma_{\tilde{\nu}}$ and C_{b2} are constants and ν is the molecular kinematic viscosity.

Turbulent viscosity

The turbulent viscosity μ_t is computed from

$$\frac{u}{u_\tau} = \frac{1}{\kappa} \ln E\left(\frac{\rho u_\tau y}{\mu}\right) \mu_t = \rho \tilde{v} f_{v1} \tag{2.18}$$

where the viscous damping function, f_{v1}, is given by

$$f_{v1} = \frac{x^3}{x^3 + C_{v1}^3} \tag{2.19}$$

and

$$\chi = \frac{\tilde{v}}{v} \tag{2.20}$$

Modeling the turbulent production

The production term G_v is modeled as

$$G_v = C_{b1} \rho \tilde{S} \tilde{v} \tag{2.21}$$

Where

$$\tilde{S} = S + \frac{\tilde{v}}{\kappa^2 d^2} f_{v2} \tag{2.22}$$

and

$$f_{v2} = 1 - \frac{\chi}{1 + \chi f_{v1}} \tag{2.23}$$

C_{b1} and κ are constants, d is the distance from the wall, and S is a scalar measure of the deformation tensor.

Modeling the turbulent destruction

The destruction term is modeled as

$$Y_v = C_{w1} \rho f_w \left(\frac{\tilde{v}}{d}\right)^2 \tag{2.24}$$

Where

$$f_w = g\left[\frac{1+C_{w3}^6}{g^6+C_{w3}^6}\right]^{1/6} \tag{2.25}$$

$$g = r + C_{w2}\left(r^6 - r\right) \tag{2.26}$$

$$r \equiv \frac{\tilde{v}}{\tilde{S}\kappa^2 d^2} \tag{2.27}$$

C_{w1}, C_{w2} and C_{w3} are constants, and $\tilde{S}$ is given by Equation (2.22). Note that the modification described above to include the effects of mean strain on S will also affect the value of $\tilde{S}$ used to compute r.

Model constants

The model constants $C_{b1}, C_{b2}, \sigma_{\tilde{v}}, C_{v1}, C_{w1}, C_{w2}, C_{w3}$ and κ have the following default values

C_{b1}=0.1335, C_{b2}=0.622, $\sigma_{\tilde{v}}$=2/3, C_{v1}=7.1,

$C_{w1} = C_{b1}/\kappa^2 + \left(1+C_{b2}\right)/\sigma_{\tilde{v}}$, C_{w2}=0.3, C_{w3}=2.0

κ=0.41

Wall boundary conditions

At walls, the modified turbulent kinematic viscosity $\tilde{v}$ is set to zero.

When the mesh is fine enough to resolve the laminar sub layer, the wall shear stress is obtained from the laminar stress-strain relationship:

$$\frac{u}{u_\tau} = \frac{\rho u_\tau y}{\mu} \tag{2.28}$$

If the mesh is too coarse to resolve the laminar sublayer, it is assumed that the centroid of the wall-adjacent cell falls within the logarithmic region of the boundary layer, and the law-of-the-wall is employed:

$$\frac{u}{u_\tau} = \frac{1}{\kappa} \ln E \left(\frac{\rho u_\tau y}{\mu} \right) \tag{2.29}$$

where κ=0.419 and $E = 9.793$.

2.2.4 SST turbulence model (Menter, 1994)

A major boundary layer effect is the separation from a surface under adverse pressure gradient conditions. Separation has a strong effect on the near-wall turbulence and therefore on the turbulent heat transfer. The SST model has demonstrated the capability of accurate separation predictions in numerous cases, (Bardina et al., 1997) and is used as the basis for heat transfer predictions by the present authors. The idea behind the SST model is to combine the best elements of the k-ε and the k-ω model with the help of a blending function F_1. F_1 is one near the surface and zero in the outer part and for free shear flows. It activates the Wilcox model in the near-wall region and the *k*-ε model for the rest of the flow. By this approach, the attractive near-wall performance of the Wilcox model can be utilized without the potential errors resulting from the free stream sensitivity of that model.

The formulation of the SST model is as follows:

$$\frac{\partial(\rho k)}{\partial t} + \frac{\partial(\rho U_j k)}{\partial x_j} = \widetilde{P}_k - \beta^* \rho \omega k + \frac{\partial}{\partial x_j}\left(\Gamma_k \frac{\partial k}{\partial x_j} \right) \tag{2.30}$$

$$\frac{\partial(\rho \omega)}{\partial t} + \frac{\partial(\rho U_j \omega)}{\partial x_j} = \frac{\gamma}{\nu_t} P_k - \beta \rho \omega^2 + \frac{\partial}{\partial x_j}\left(\Gamma_\omega \frac{\partial \omega}{\partial x_j} \right) + (1 - F_1) 2 \rho \sigma_{\omega 2} \frac{1}{\omega} \frac{\partial k}{\partial x_j} \frac{\partial \omega}{\partial x_j} \tag{2.31}$$

with

$$\Gamma_k = \mu + \frac{\mu_t}{\sigma_k}, \Gamma_\omega = \mu + \frac{\mu_t}{\sigma_\omega}, \quad P_k = \tau_{ij} \frac{\partial U_i}{\partial x_j}, \quad \widetilde{P}_k = \min(P_k; C_1 \varepsilon) \tag{2.32}$$

The coefficients, φ , of the model are functions of F_1: φ = $F_1 \varphi_1$ + (1−$F_1)\varphi_2$, where φ_1, φ_2 stand for the coefficients of the k-ω and the k-ε model respectively:

$\sigma k_1 = 2.000, \sigma\omega_1 = 2.000, \kappa = 0.41, \gamma_1 = 0.5532, \beta_1 = 0.0750, \beta^* = 0.09, C_1 = 10$

$\sigma k_2 = 1.000, \sigma\omega_2 = 1.168, \kappa = 0.41, \gamma_2 = 0.4403, \beta_2 = 0.0828, \beta^* = 0.09$

with $F_1 = \tanh(\arg_1^4)$, $$\arg_1 = \min\left(\max\left(\frac{\sqrt{k}}{\beta^*\omega y};\frac{500\nu}{y^2\omega}\right);\frac{4\rho\sigma_{\omega 2}k}{CD_{k\omega}y^2}\right) \quad (2.33)$$

$$CD_{k\omega} = \max\left(2\rho\sigma_{\omega 2}\frac{1}{\omega}\frac{\partial k}{\partial x_j}\frac{\partial \omega}{\partial x_j};1.0e^{-10}\right) \quad (2.34)$$

$$F_2 = \tanh(\arg_2^2) \qquad \arg_2 = \max\left(2\frac{\sqrt{k}}{\beta^*\omega y};\frac{500\nu}{y^2\omega}\right) \quad (2.35)$$

$$\tau_{ij} = \mu_t\left(\frac{\partial U_i}{\partial x_j}+\frac{\partial U_j}{\partial x_j}-\frac{2}{3}\frac{\partial U_k}{\partial x_k}\right)-\frac{2}{3}\rho k\delta_{ij} \quad (2.36)$$

An additional feature of the SST model is the introduction of an upper limit for the turbulent shear stress in boundary layers in order to avoid excessive shear-stress levels typically predicted with Boussinesq eddy-viscosity models. The eddy viscosity is defined as:

$$\mu_t = \rho\frac{a_1 k}{\max(a_1\omega;\sqrt{2}S\cdot F_2)} \quad (2.37)$$

with a_1 = 0.31. Again F_2 is a blending function (described in Eq. 2.35) similar to F_1, which restricts the limiter to the wall boundary layer, as the underlying assumptions are not correct for free shear flows. The only difference to the original formulation given by Menter (1994) is that the absolute value of the strain rate $S = \sqrt{S_{ij}S_{ij}}$, is now used in the definition of the eddy viscosity instead of the vorticity in order to increase the generality of the method beyond aerodynamic applications. In addition, the limiter in the production rate is used with a limiting value of C_l=10 in all SST model simulations. This eliminates the build-up of turbulence in stagnation regions of airfoils or turbine blades etc. Note that there is a strong similarity between the production limiter used in the SST model and the realizability constraint imposed in the v2f model.

The v2f limiter reads:

$$\nu_t = \widetilde{c_\mu}\overline{\nu^2}T; \quad T = \min\left(\frac{k}{\varepsilon}; \frac{0.6}{\sqrt{6}} \frac{k}{\overline{\nu^2}\widetilde{c_\mu}S}\right)$$

it can be re-formulated as follows:

$$\nu_t = \nu_t \min\left(1; 1.15 \cdot \frac{\varepsilon}{P_k}\right)$$

for boundary layer flows. This has to be compared with the re-written production limiter of the SST model:

$$\widetilde{\nu_t} = \nu_t \min\left(1; 10 \cdot \frac{\varepsilon}{P_k}\right)$$

which is only used in the production term of the *k*-equation. It is clear that the V2f limiter is much more restrictive and can have a significant effect on the performance of the underlying turbulence model, particularly for adverse pressure gradient flows where ε/P_k can be much smaller than 1.15. The limiter can therefore be activated in regions where realizability is not at stake. It serves therefore a similar purpose as the SST limiter given by Equation (2.37).

In analogy to the modeling of the turbulent stress tensor, the turbulent heat flux vector is modeled with the help of a turbulent diffusivity:

$$\overline{U'_i T'} = -\varepsilon \frac{\partial T}{\partial x_i} = -\frac{\nu_t}{\Pr_t} \frac{\partial T}{\partial x_i} \quad \text{with } \Pr_i = \frac{\nu_t}{\varepsilon_h} \tag{2.38}$$

In the absence of source terms and under constant property assumptions, the temperature equation is therefore written as:

$$\frac{\partial \rho T}{\partial T} + \frac{\partial \rho U_j T}{\partial x_j} = \frac{\partial}{\partial x_j}\left[\left(\frac{\mu}{\Pr} + \frac{\mu_t}{\Pr_i}\right)\frac{\partial T}{\partial x_j}\right] \tag{2.39}$$

The Prandtl number $\Pr$ is a fluid property, and the turbulent Prandtl number, $\Pr_t$ is set to a constant value, assuming an analogy between turbulent heat and mass transfer. Experiments and analysis, place the turbulent Prandtl number in the range of 0.9, which is also used in the present formulation.

The advantage of the SST over the k-ε model can be seen for adverse pressure gradient conditions. The results reported by Menter (1994) demonstrate the superior performance of the SST model for separated flows.

2.3 The cavitation model by Zwart et al. (2004).

2.3.1. Governing equations

The equations governing multiphase flow include conservation of mass for each phase

$$\frac{\partial(\rho_\alpha r_\alpha)}{\partial t} + \frac{\partial(\rho_\alpha r_\alpha u_i)}{\partial x_i} = \dot{S}_\alpha \tag{2.40}$$

and conservation of momentum for the mixture (assuming no interphase slip):

$$\frac{\partial(\rho_m u_i)}{\partial t}+\frac{\partial(\rho_m u_i u_j)}{\partial x_i}=-\frac{\partial P}{\partial x_i}+\rho_m r_\alpha g_i+\frac{\partial(\tau_{ji})}{\partial x_j} \tag{2.41}$$

where:

ρ_α Density of phase α ;

r_α Volume fraction of phase α ;

u_i Cartesian velocity components;

$\dot{S}_\alpha$ Mass generation rate of phase α ;

ρ_m Volume-weighted mixture of density;

g_i Acceleration due to gravity;

P Pressure;

τ_{ji} Stress tensor, related to the deformation rates using Stokes' law:

$$\tau_{ji}=\mu_m\left(\frac{\partial u_i}{\partial x_j}+\frac{\partial u_j}{\partial x_i}\right) \quad , \tag{2.42}$$

and μ_m is the volume-weighted mixture of viscosity.

The mass sources have the constrain that:

$$\sum_{\alpha=1}^{N}\dot{S}_\alpha=0 \quad , \tag{2.43}$$

and the volume fraction of the two phases (liquid and gas, or vapor):

$$\sum_{\alpha=1}^{N}r_\alpha=1 \tag{2.44}$$

Equations 2.40, 2.41 and 2.44 are a closed system involving (N+4) equations and (N+4) unknowns, N being the number of phases.

2.3.2. Cavitation modeling

Zwart et al. (2004) used a reduced form of the well known Rayleigh-Plesset equation (2.45) below, which describes growth and collapse of a single bubble

$$R\ddot{R}+\frac{3}{2}\left(\dot{R}\right)^{2}=\frac{P_{v}-P}{\rho_{L}}+\frac{P_{Go}}{\rho_{L}}\left(\frac{R_{o}}{R}\right)^{3k}-\frac{4\mu_{L}\dot{R}}{\rho_{L}R}-\frac{2\sigma_{L}}{\rho_{L}R} \tag{2.45}$$

Where in equation (2.45),

R is the bubble radius;

$$\dot{R}=\frac{dR}{dt},\ddot{R}=\frac{d^{2}R}{dt^{2}}$$

P_v is the vapor pressure;

P is the pressure outside the bubble;

ρ_L is the liquid density;

P_{Go} is the initial gas pressure inside the bubble;

R_0 is the initial bubble radius at time t = 0;

k is a constant, where k = 1 implies constant bubble temperature and k=γ in case of adiabatic flow.

σ_L is the liquid surface tension coefficient

μ_L is the viscosity of the liquid.

Zwart et al. (2004) neglected the second-order term as well as the terms representing the effect of viscosity, surface tension, and gas inside the bubble. This simplification of equation (2.45) results into the following simplified expression for bubble wall velocity

$$\frac{dR_B}{dt} = \sqrt{\frac{2}{3}\frac{P_v - P}{\rho_L}} \tag{2.46}$$

The value of $\frac{dR_B}{dt}$ calculated from equation (2.46) is used to calculate the mass source term $\dot{S}_\alpha$ for vapor phase in equation (2.40).

The rate of change of volume of a single bubble can be calculated with the help of equation (2.46) as,

$$\frac{dV_B}{dt} = \frac{d}{dt}\left(\frac{4}{3}\pi R^3\right) = 4\pi R^2\sqrt{\frac{2}{3}\frac{P_v - P}{\rho_L}} \tag{2.47}$$

The rate of change of mass of a single bubble can be calculated using equation (2.47) as:

$$\frac{dm_B}{dt} = \rho_v\frac{dV_B}{dt} = 4\pi R^2\rho_v\sqrt{\frac{2}{3}\frac{P_v - P}{\rho_L}} \tag{2.48}$$

If there are N_B bubbles per unit volume, the vapor volume fraction is expressed as, $N_B r_v$,

$$r_v = V_B N_B = \frac{4}{3}\pi R^3 N_B \tag{2.49}$$

and the total inter phase mass transfer rate due to cavitation per unit volume is defined as:

$$\dot{S}_v = N_B\frac{dm_B}{dt} = \frac{3r_v\rho_v}{R_B}\sqrt{\frac{2}{3}\frac{P_v - P}{\rho_L}} \tag{2.50}$$

As this model has been derived assuming bubble growth (vaporization). It can be generalized to include condensation as follows:

$$\dot{S}_v = C\frac{3r_v\rho_v}{R_B}\sqrt{\frac{2}{3}\frac{|P_v - P|}{\rho_L}}sign(P_v - P) \tag{2.51}$$

where C is an empirical calibration coefficient.

In Zwart et al. (2004), the source terms for vaporization and condensation are given by:

$$\dot{S}_v = C_{cond}\frac{3r_v\rho_v}{R_B}\sqrt{\frac{2}{3}\frac{P-P_v}{\rho_L}}, \text{ if } P > P_v$$

$$\dot{S}_v = C_{vap}\frac{3r_{nuc}(1-r_v)\rho_v}{R_B}\sqrt{\frac{2}{3}\frac{P_v-P}{\rho_L}}, \text{ if } P < P_v \tag{2.52}$$

In the simulations reported by Zwart et al. (2004) the values of the initial bubble radius and the empirical constants and are:

$$R_B = 10^{-6}m, r_{nuc} = 5\times10^{-4}, C_{vap} = 50, C_{cond} = 0.01 \text{ and}, C_{cond} = 0.01$$

2.4 Initial and boundary conditions

In our simulations, wall boundary conditions were set on blade, shell, and hub surfaces. This condition specifies a velocity of zero on these surfaces and the flow can not cross the boundary surface. As the flow field is repeated around each blade element, rotational periodic boundary conditions were applied on surfaces in the tangential direction. These surfaces allow the flow out from one boundary to enter the corresponding boundary. A stage sliding interface was applied at the interface between each element of the torque converter using a conservative mixing plane approach.

Chapter 3 Results and Discussion

3.1 Introduction

In order to evaluate the effects of different factors in predicting cavitation by using ANSYS CFX10.0, a large number of simulations were carried out both in the steady and the transient state.

The commercial package ANSYS-CFX is a finite-volume based CFD package with second order accuracy in space and time and an algebraic multi-grid technique. ANSYS-CFX is an integrated software system capable of solving diverse and complex three-dimensional fluid flow problems. The multi-grid based fluid flow solver provides solutions for incompressible and compressible, steady-state and transient, laminar and turbulent, single and multiphase, and thermal fluid flow problems in complex geometries. The software uses unstructured and block-structured non-orthogonal grids with grid embedding and grid attaching to discretize the domain.

3.2 The use of Zwart's model (2004)

3.2.1 Single phase results

This section presents the validation of the numerical solution by simulating single phase flow in two torque converters. First torque converter has a diameter of 245 mm, with 32 pump blades, 36 turbine blades, and 17 stator blades; the second torque converter has a diameter of 258 mm, with 31 pump blades, 29 turbine blades, and 18 stator blades. The performance parameters which are K-factor, torque ratio, and efficiency were calculated and compared with experimental data.

3.2.1.1 Simplifying assumptions

The following assumptions were used during simulation:

1. Flow was assumed to be steady.

2. Single blade of each element has been simulated due to the periodicity of elements. Figure 3.1 shows a pump element containing a blade and two periodic surfaces.

3. The fluid was incompressible.

4. The fluid flow was simulated at a constant temperature, no heat transfer was considered.

5. The standard k-ε model was used to simulate turbulence in the flow.

6. Turbo machinery mixing plane method was used.

7. Only single phase fluid was modeled by assuming that there was no cavitation in the torque converter.

8. Both leakage flow and cooling flow have been neglected.

3.2.1.2 Mesh generation

The mesh was generated using CFX-Turbogrid software. Three meshes were used, which were coarse, medium and fine meshes. The coarse mesh had 60,000 elements and was used to test the correctness of the boundary conditions used. The medium mesh had about 200,000 elements, while the fine mesh had about 500,000 elements. Figure 3.2 shows a torque converter CFD mesh model. Only hexahedral type cells were used as it was found to result in the best convergence and accuracy.

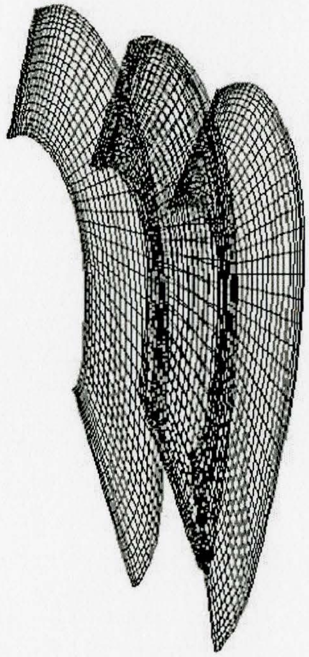

Figure 3.1. Pump blade and periodic surface

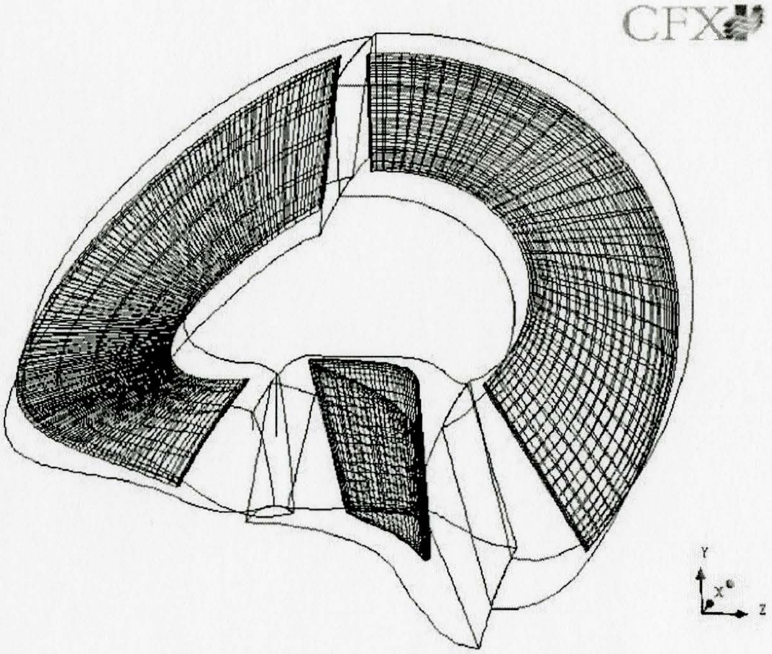

Figure 3.2. Torque converter mesh

Figure 3.3 shows variation of the K-factor with mesh size, it indicates that the difference in the K-factor between medium and fine meshes is about 0.5%. The fine mesh was used in the present study.

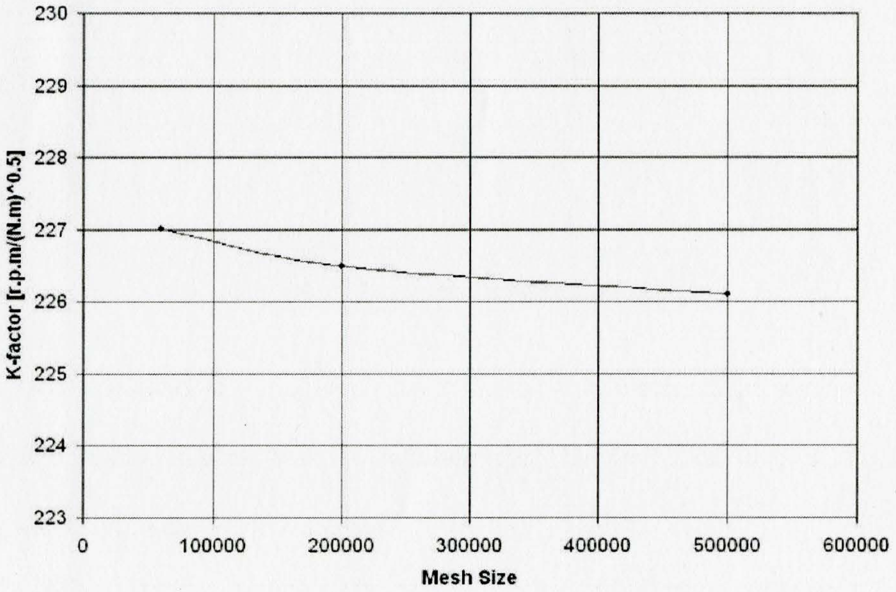

Figure 3.3. Effect of grid mesh on K-factor at speed ratio 0.4

3.2.1.3 Simulation set up

Simulation is carried out using CFD package CFX 10.0. The flow solver is based on finite-volume method solving three-dimensional Navier-Stokes equations for incompressible, steady, or transient state, laminar, or turbulent flow. The torque converter flow field has been solved at different speed ratios. The pump speed is adjusted to insure that pump torque is 100 lb.ft (135 N.m) as in the experiments conducted by GM. Computations were stopped when residual of flow field (u, v, w) and pressure field were less than 1×10^{-4}. Convergence of the model was also checked by examining the following three parameters:

- Conservation of mass across each element, i.e., mass flow in is equal to mass flow out.

- Difference between the calculated torque using CFX and using Euler's equation is less than 1%.

- Torque imbalance in torque converter. Torque of turbine is equal to pump torque and stator torque. The calculated torque shows imbalance of about 0.1% using the fine mesh.

3.2.1.4 Numerical results for torque converter 245 mm

Simulation was done at five speed ratios 0.065, 0.2, 0.4, 0.6 and 0.8. The following section shows a comparison between numerical results and experimental results.

The dynamometer data was acquired from GM, USA. The experimental performance parameters were compared with numerical results (Fig. 3.4). The comparison shows a good agreement between experimental and numerical data.

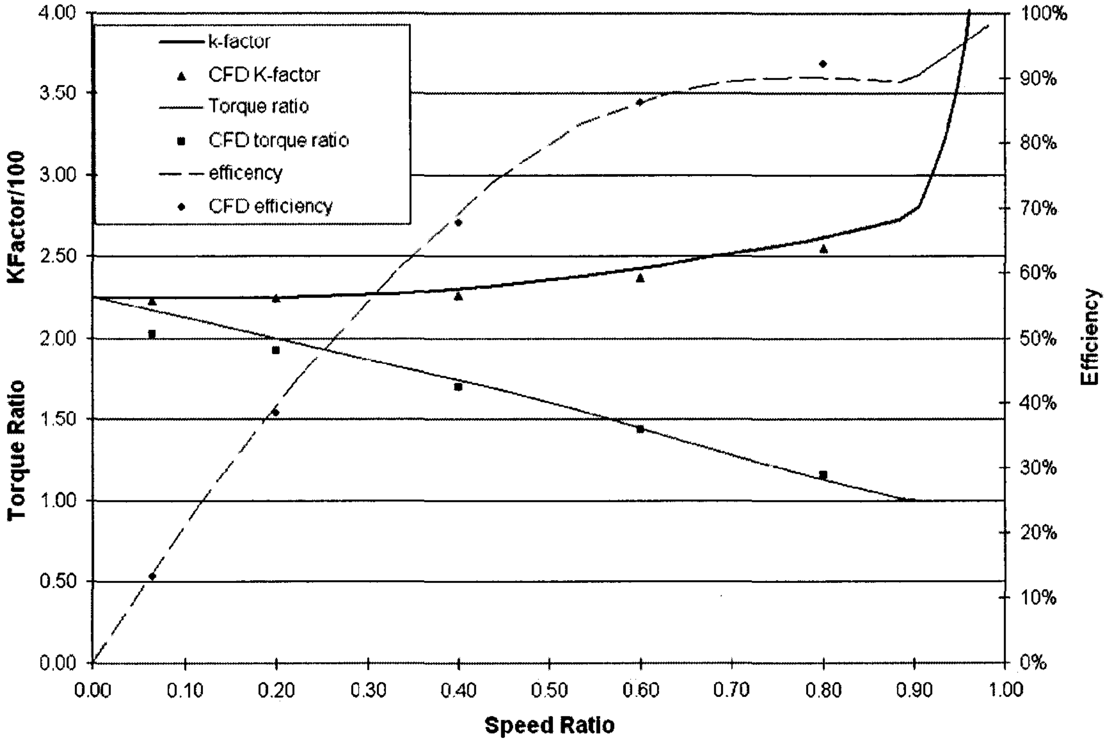

Figure 3.4. Torque converter 245 mm performance comparison with experiments.

3.2.1.5 Numerical results for torque converter 258 mm

For torque converter 258 mm simulation was run at six speed ratios 0.0, 0.229, 0.555, 0.775, 0.858 and 0.913. The following figure shows a comparison between numerical results and experimental results.

The dynamometer data was acquired from GM, USA. Figure 3.5 shows a comparison between experimental performance parameters results and numerical results. The comparison shows a good agreement between experimental and numerical data.

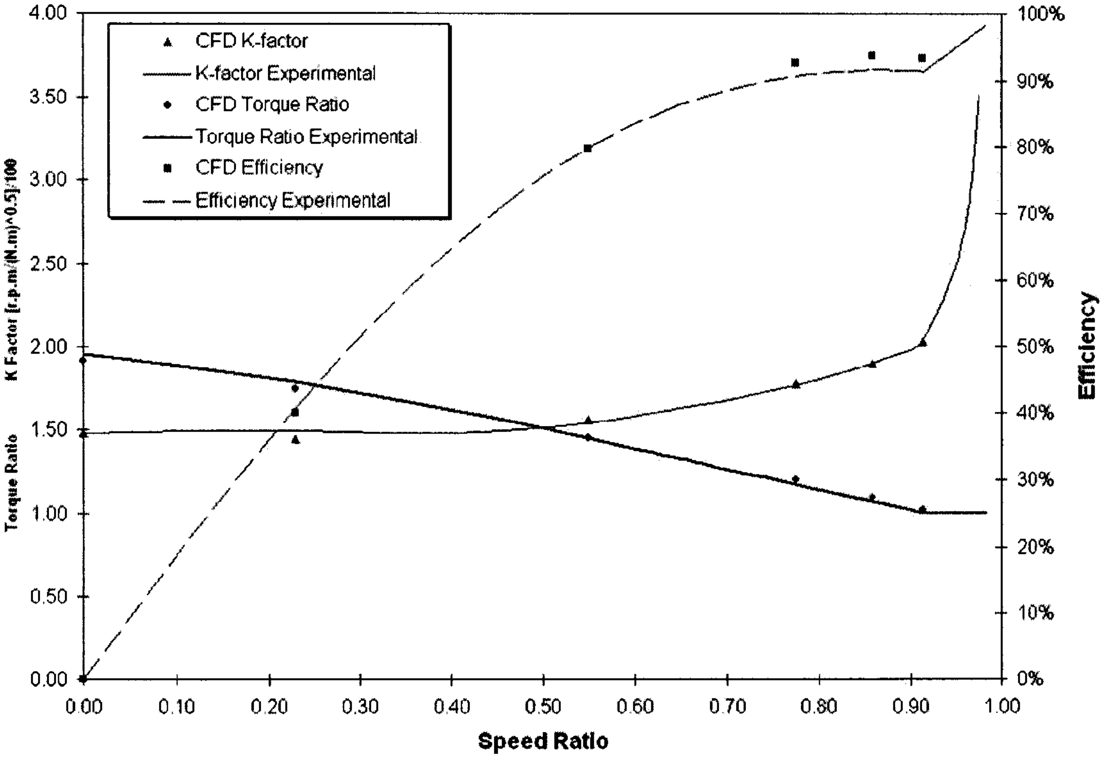

Figure 3.5. Torque converter 258 mm performance comparison with experiments.

3.2.1.6 Cavitation possibility investigation

The results from the single phase simulations were used to study possibility of cavitation occurrence in torque converter by identifying locations of low pressures. The most severe operating condition for cavitation in torque converter is at stall i.e. at speed ratio equal zero. Two simulations were done at different pump speeds and same transmission supply pressure.

Figures 3.6 and 3.7 show blade-to-blade views of pressure calculated at a plane between shell and core at span = 50% for torque converters 245 mm and 258 mm, respectively. Figure 3.6(a) shows pressure distribution at pump speed 1600 rpm for torque converter 245 mm. There is small area of zero pressure at the nose of the stator blades. This area increased as pump speed increased to 2000 rpm (Fig. 3.6(b)). This area indicated possibility of cavitation existence with increasing of pump speed. Figure 3.7(a) shows pressure distribution at pump speed 1600 rpm for torque converter 258 mm. There is a small area of zero pressure at the nose of the stator blades and at inlet edge of turbine blades. These areas increased as pump speed increased to 2000 rpm (Fig. 3.7(b)), which may also lead to cavitation.

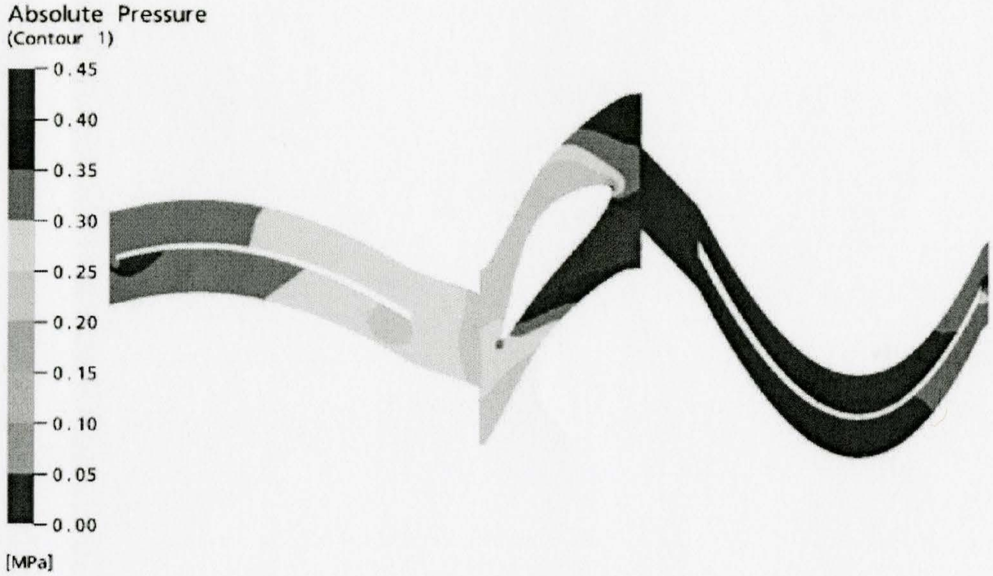

(a) pump speed= 1600r.p.m, turbine speed = 0 r.p.m, transmission pressure = 40 psi

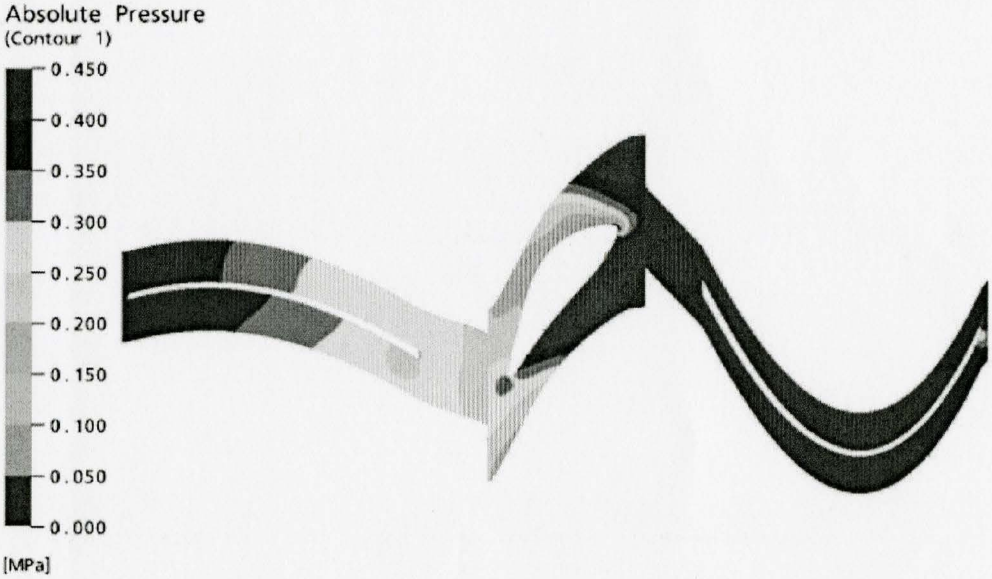

(b) pump speed= 2000 r.p.m, turbine speed = 0 r.p.m, transmission line pressure = 40 psi

Figure 3.6. CFD data of absolute pressure in torque converter 245 mm

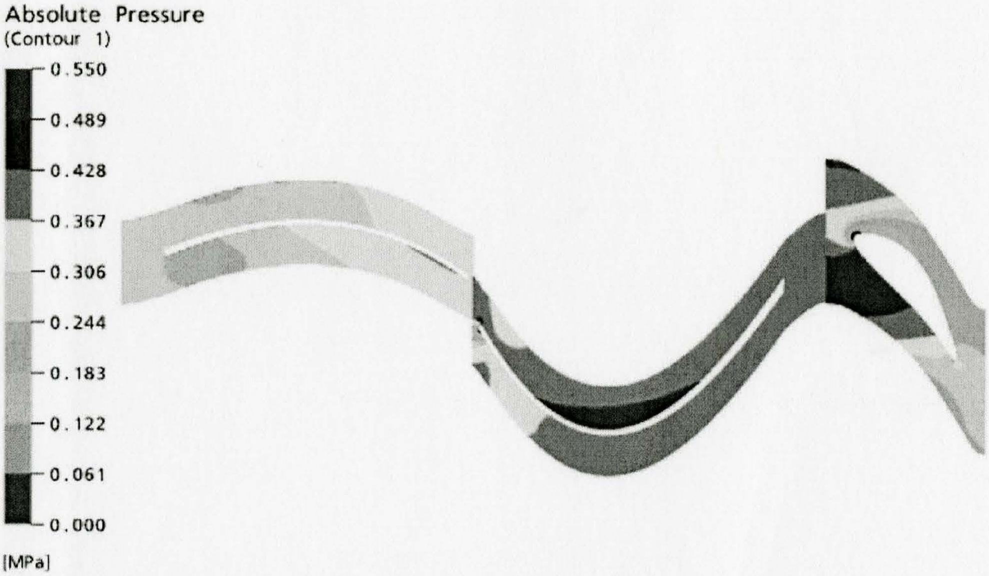

(a) pump speed= 1600r.p.m, turbine speed = 0 r.p.m, transmission line pressure = 40 psi

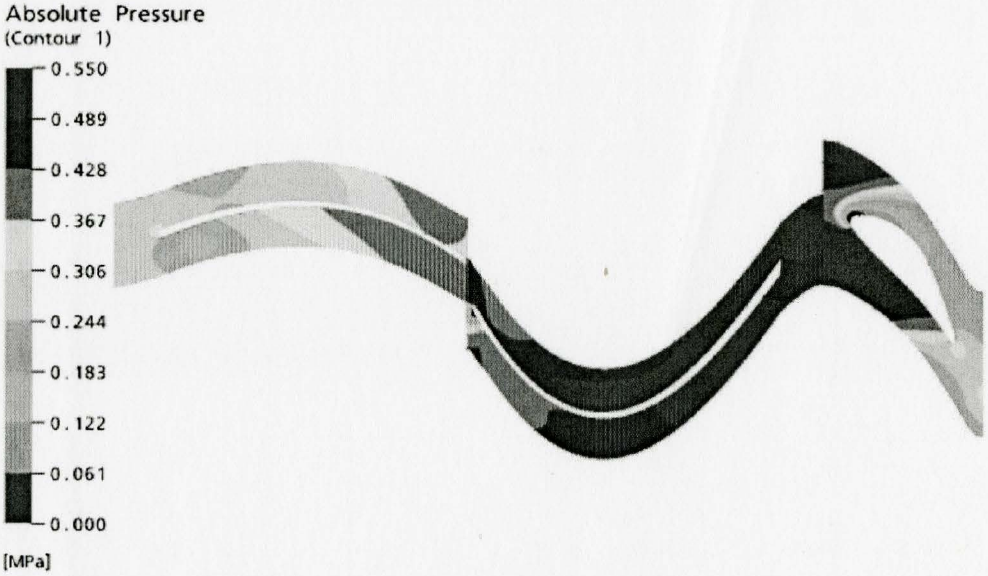

(b) pump speed= 2000 r.p.m, turbine speed = 0 r.p.m, transmission line pressure = 40 psi

Figure 3.7. CFD data of absolute pressure in torque converter 258 mm

3.2.2 Grid test

All simulations were run using stage averaging between the torque converter elements to obtain steady state solutions. The effect of grid density on the numerical results was investigated. The three different grids considered in this study were a coarse grid of 332,400 elements, a medium grid of 703,360 elements and a fine grid of 1,013,920 elements. Results obtained using the coarse grid showed a significant difference in torque imbalance, T_u, defined as:

$$T_u = T_t - \left(T_p + T_s\right)$$

Where:

T_t is the turbine torque, T_p is the pump torque, and T_s is the stator torque.

Although the coarse grid gave good results in terms of values of torque imbalance in the case of single phase flows, i.e., with no cavitation, this grid in the case of multi-phase flows, i.e., with cavitation, produced a large torque imbalance with respect to pump input torque. The value of torque imbalance ranged from 21% to 43% for the various pump speeds simulated, which is too high compared with less than 1% imbalance in the cases of medium and fine grids.

Figure 3.8 is a plot of pump torque versus pump speed at stall operating condition comparing experimental results reported in Anderson et al. (2003) to numerical results using three different grid sizes. As expected, the torque increases as the pump speed increases. The numerical results obtained using both the medium and the fine grids are very close to each other indicating that with the medium size mesh and finer, numerical results are not too sensitive to changes in grid size. Excluding the coarse mesh results, there is excellent agreement between the numerical results and the experimental data at pump speed of 2000 rpm. However, numerical results diverge from the experimental data as the pump speed increases to levels where cavitation is likely to occour.

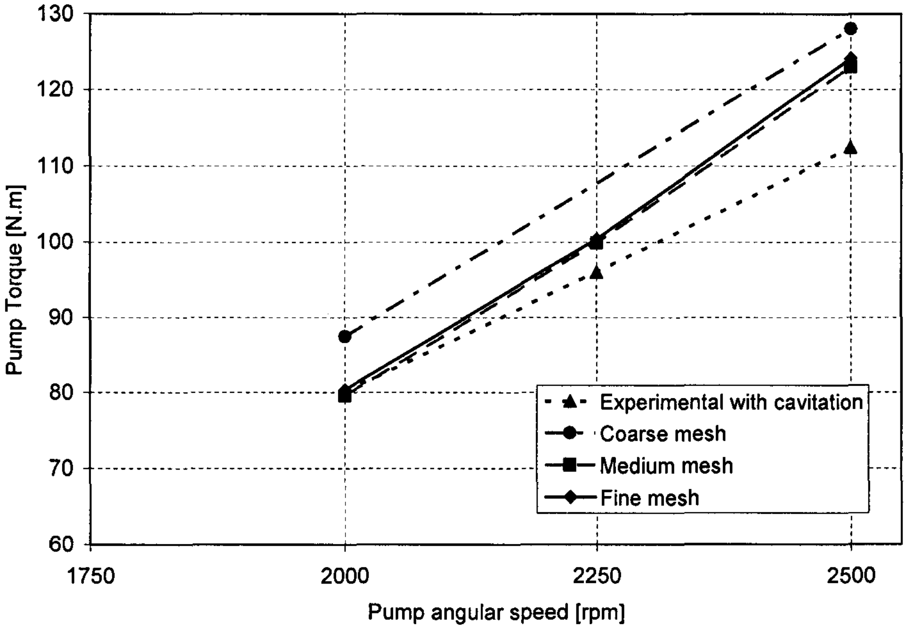

Figure 3.8. Stall pump torque at various pump speeds and charge pressure = 70 psi. A comparison between the present numerical results and experimental results reported in Anderson et al. (2003)

K-factors were calculated from the data in Figure 3.8 to create the plot in Figure 3.9. For medium and fine mesh and at the low pump speed 2000 rpm, the numerically determined K-factors agree well with the K-factor calculated from test data. At the higher pump speeds, Figure 3.9 shows that the numerical K-factors (defined as $K = \frac{\Omega_p}{\sqrt{T_p}}$) are much lower than those determined experimentally. This indicates that the numerical solution is unable to capture the effect of the cavitation inside the torque converter which causes a significant decrease in pump torque and corresponding increase in K-factor. Plotting the data in K-factor format enables comparison of scaled test results from similar converters of different sizes.

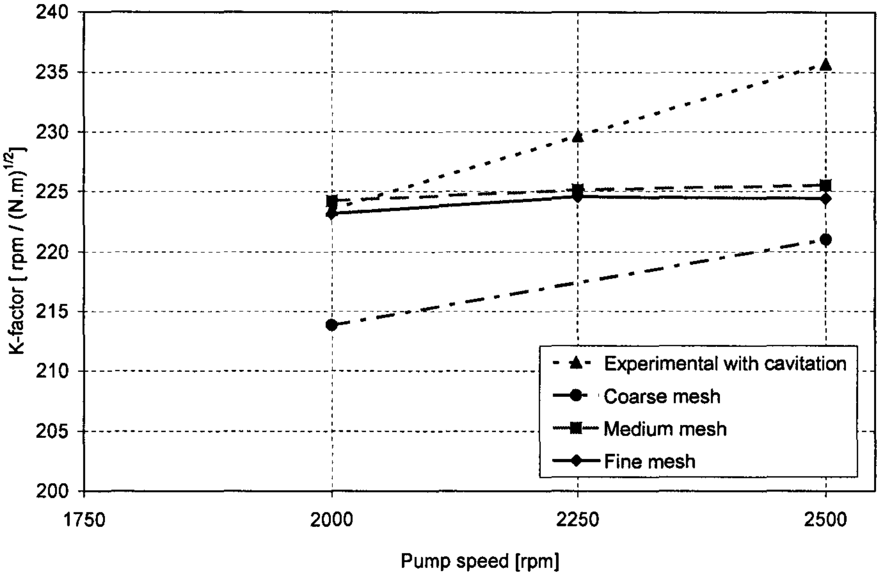

Figure 3.9. Stall K-factor at various pump speeds and charge pressure = 70 psi. A comparison between numerical results and the experimental results reported in Anderson et al. (2003)

Figure 3.10 contains a plot of K-factor versus pump speed for experimental and CFD results with and without cavitation. The experimental data is from Anderson et al. (2003) for the with cavitation case and from General Motors Inc. for the case without cavitation. The experimental data without cavitation was generated by scaling test results from a geometrically similar torque converter of much larger diameter. The relatively constant K-factor values indicate that the larger diameter converter did not experience cavitation at the tested pump speeds. Figure 3.10 shows that the numerical results obtained using the cavitation model are very close to the experimental results from the converter without cavitation. The CFD with cavitation solution obtained at pump speed of 2500 rpm shows a small increase in the K-factor, but the increase is significantly lower than the experimental values determined by Anderson (2003). This difference in the K-factor indicates that the current cavitation model implemented in ANSYS-CFX 10.0 is not able to capture the full effect of cavitation inside a torque converter. The numerical results presented here for the case with cavitation were obtained using the default values of the two empirical constants suggested by Zwart et al. (2004).

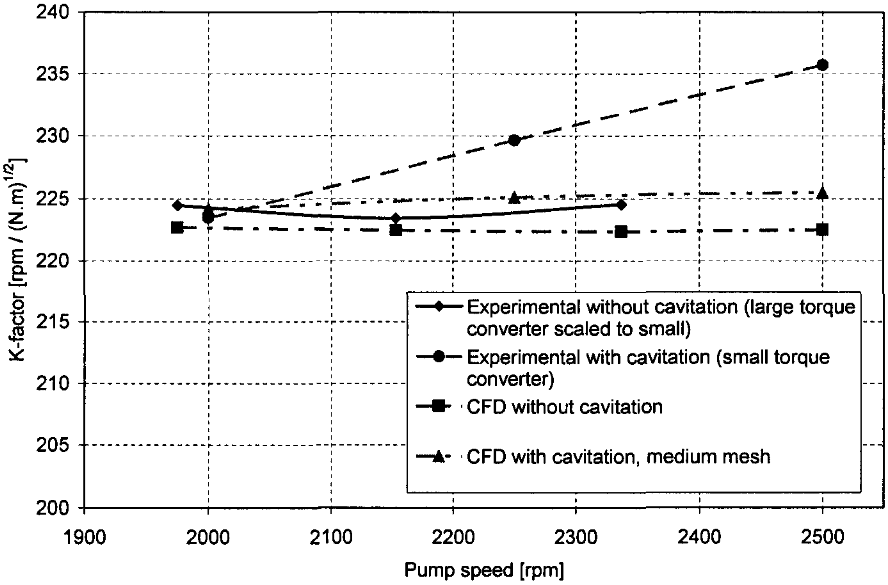

Figure 3.10. Stall K-factor versus pump speed. A comparison between numerical and experimental results obtained from GM for the large diameter torque converter and from the experimental results reported in Anderson et al. (2003)

3.2.3 Effect of model constants

3.2.3.1 Vapor volume fraction at different pump speeds.

Figure 3.11 shows the distribution of vapor volume fraction (VVF) around the stator nose at three different pump speeds, 2000, 2250 and 2500 rpm. At pump speed of 2500 rpm, a bigger area of VVF is produced as compared with those produced at the lower speeds. Similar to the results for pressure distribution, the model was able to predict an increase in the VVF for the higher pump speed, but the increase was not large enough to cause a noticeable effect on converter performance, as indicated by the K-factor values.

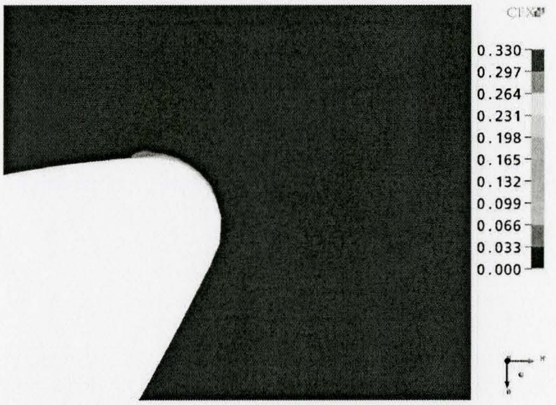

(a)

(b)

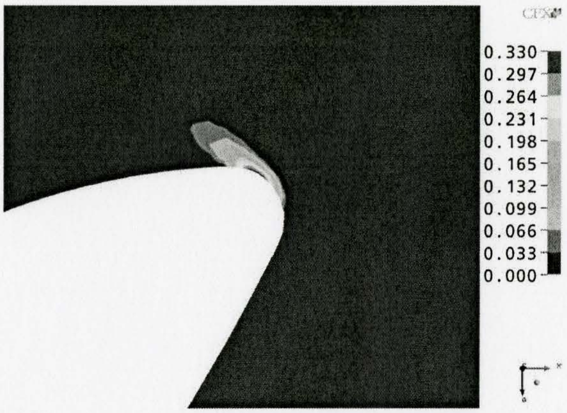

(3)

Figure 3.11. Vapor volume fraction around the stator nose at a plane midway between the shroud and hub at (a) Pump speed = 2000 rpm, (b) Pump speed = 2250 rpm, and (c) Pump speed = 2500 rpm

3.2.3.2 Effect of the empirical coefficients.

Considering the fact that all numerical results obtained using the default values of the empirical coefficients built in ANSYS-CFX 10.0 did not produce reasonable results for a converter with cavitation, the coefficients were modified to try to arrive at the right set of values that would allow the model to produce acceptable results. Zwart et al. (2004) indicated that the values of the empirical coefficients of their cavitation model are not general, and that they have to be modified based on the problem in hand. They indicated that they tried hundreds of various combinations until they finally arrived at the right set to simulate cavitation inside a venturi. Following the same concept, many combinations of coefficients were tested until the right set was found for the modeled torque converter. The evaporation empirical coefficient C_{vap} was modified from 50 to 50000, and the empirical condensation coefficient C_{cond} from 0.01 to 1×10^{-6}. Figure 3.12 shows the resulting VVF formation over the stator nose of the torque converter using the default and the modified empirical coefficients. With the proposed values, a bigger area of VVF formed at the stator nose. This area was big enough to restrict the flow through the stator and hence resulted in a significant drop in the pump torque which caused the K-factor to increase. A K-factor of 233.7 was resulted from using the proposed empirical coefficients which is very close to the experimental value of 236.

Figure 3.13 shows VVF over all the converter elements using the modified coefficients. This figure shows a region of vapor over the pump blades extending to the turbine inlet. There is no vapor at the middle section of the turbine blade till its exit. This agrees with what was observed by Anderson et al. (2003) and Mekkes (2003) during their experiments on cavitation inside torque converters.

In order to better understand the reason behind this, we recall the mathematical model that Zwart (2004) developed:

$$\dot{S}_v = C\frac{3r_v\rho_v}{R_B}\sqrt{\frac{2}{3}\frac{|P_v-P|}{\rho_L}}\,sign(P_v-P) \tag{2.51}$$

$$\dot{S}_v = C_{cond}\frac{3r_v\rho_v}{R_B}\sqrt{\frac{2}{3}\frac{P-P_v}{\rho_L}}\text{, if } P>P_v$$

$$\dot{S}_v = C_{vap}\frac{3r_{nuc}(1-r_v)\rho_v}{R_B}\sqrt{\frac{2}{3}\frac{P_v-P}{\rho_L}}\text{, if } P<P_v \tag{2.52}$$

From equations (2.51) and (2.52), it is clear that if we maintain other variables constant, the interface mass transfer rate $\dot{S}_v$ will linearly depend on the set of empirical coefficients that we modified during our numerical simulation, and $\dot{S}_v$ will further effect the calculation of VVF. Physically, if we force the vaporization to dominate the whole cavitation process, but neglect the condensation, we will certainly observe a larger VVF. Hence, we would like to conclude here that VVF is strongly influenced by C_{vap} and C_{cond}, or the combination of the two, when using the only commercialized cavitation model in CFX10.0/11.0.

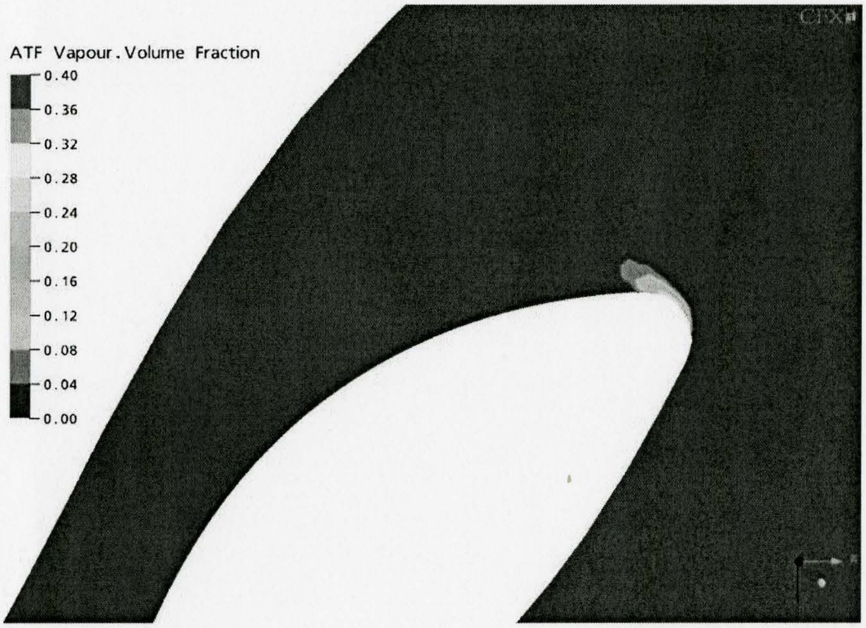

(a) Using default values of the empirical coefficients

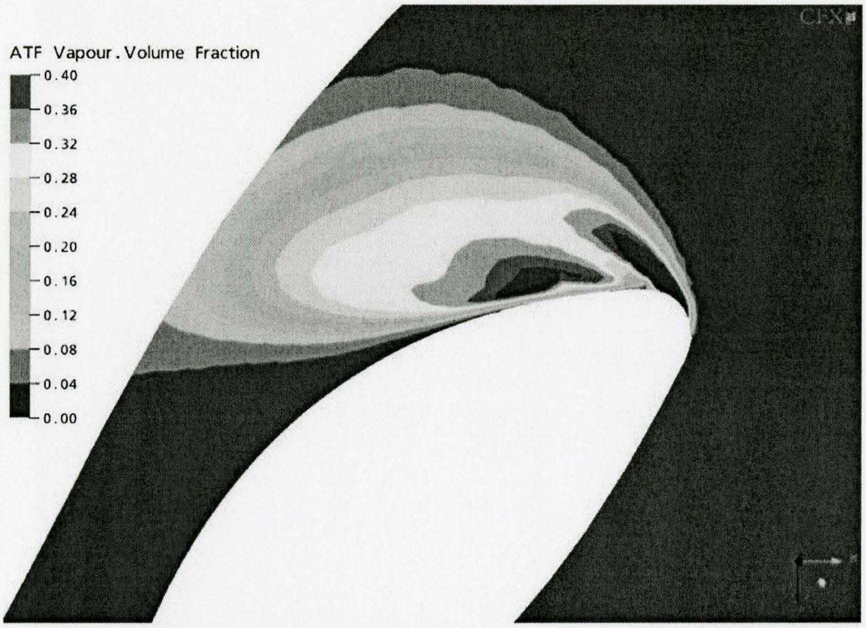

(b) Using proposed values of the empirical coefficients

Figure 3.12. Vapor volume fraction at 2500 rpm pump speed – numerical results obtained using different empirical coefficients.

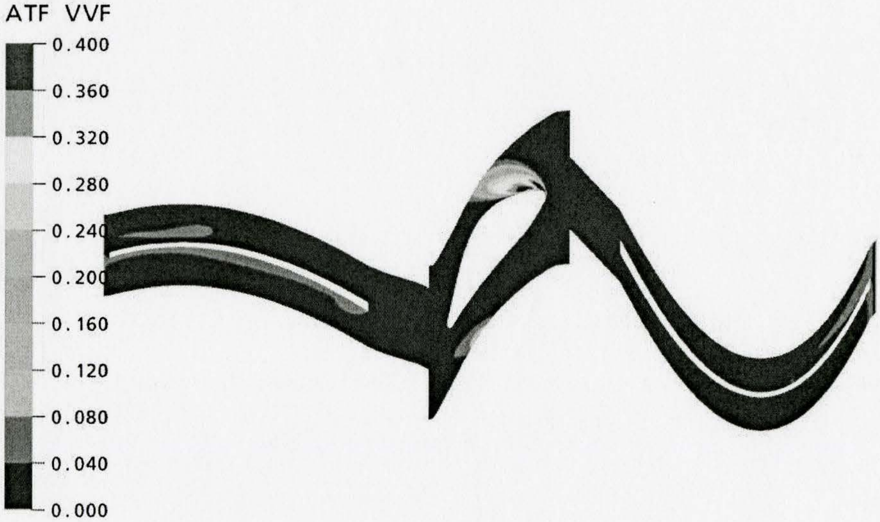

Figure 3.13: Vapor volume fraction in the pump, stator, and turbine at 2500 rpm pump speed – numerical results obtained using the proposed empirical coefficients.

It is worth mentioning here that if choosing "upwind" as the advection scheme instead of "high resolution" in the solver control, CFX will under predict the pump torque, which directly results in an increase of the K-factor. We performed a comparison to evaluate the effect of the advection scheme. Comparing to the K-factor of 233.7 we previously obtained by using "high resolution", CFX computed a K-factor of 236.4 by using "upwind" which is closer to the experimental data 236. However, instead of any increase of VVF, we observed a slight decrease of VVF as shown in figure 3.14. This comparison indicates that in the steady state, CFX tends to over predict the K-factor when using "upwind" as the advection scheme, which will be again proven to be true in the transient state.

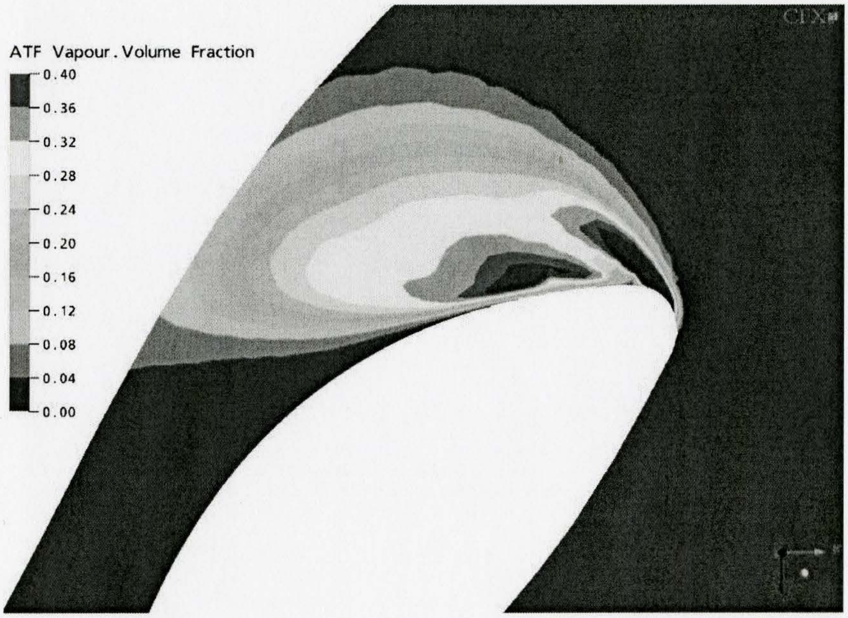

(a) Using high resolution

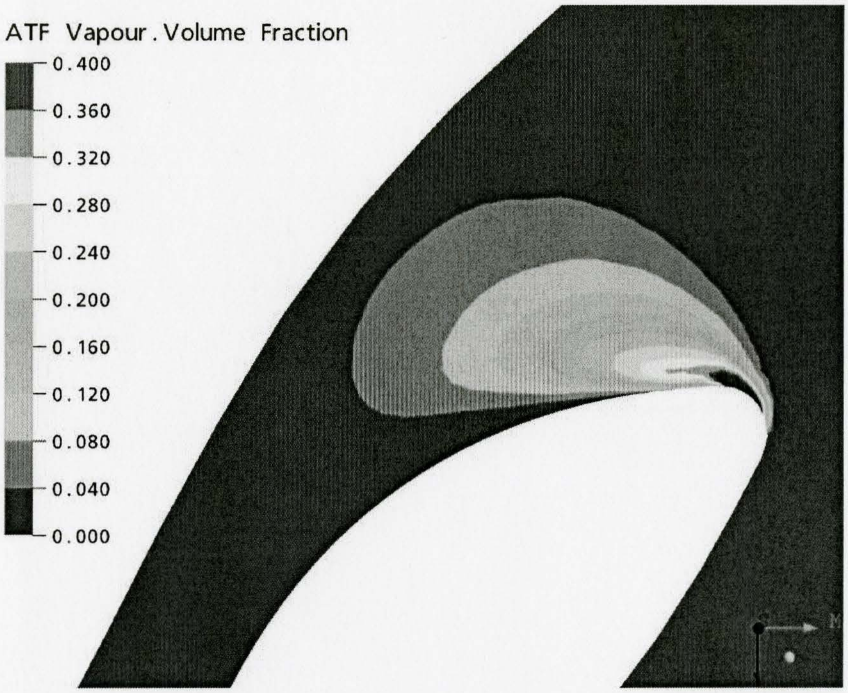

(b) Using upwind

Figure 3.14. Vapor volume fraction at 2500 rpm pump speed – numerical results obtained using proposed coefficients using different advection schemes.

3.2.3.3 Effect of vapour pressure

VVF at different pressures using the default empirical coefficients.

The value of the vapor pressure considered in all the numerical results presented so far was 200 Pa. Different authors suggested the use of other values for the vapor pressure. Brennen (1995) indicated that hydraulic oil may undergo cavitation without pressure dropping below its typical vapor pressure values. This is because hydraulic oils consist of different additives which may lead to vapor formation at pressures higher than their typical vapor pressures. Figure 3.15 shows the effect of increasing the vapor pressure on vapor formation inside the converter. Increasing the value from

200 Pa to 5000 Pa at pump speed of 2500 rpm did not result in any change in the area of VVF around the stator nose, nor did it have any effect on the torque converter performance, as evident by the value of the K-factor calculated for all the cases at 225. These vapor pressures were chosen according to the actual ATF pressures (in corresponding to the temperature ranges from 60 degree to 200 degree, see figure 3.16.) under the normal operating condition.

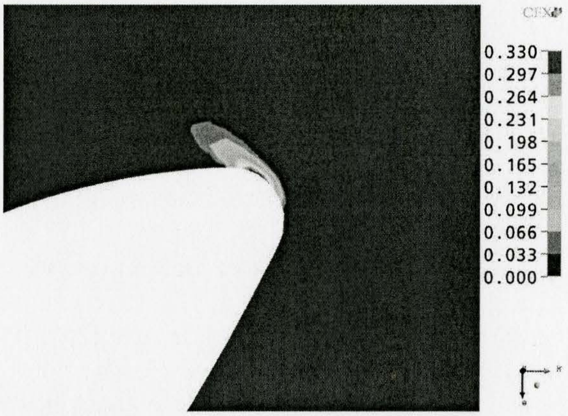

(a) $P_v = 200$ Pa

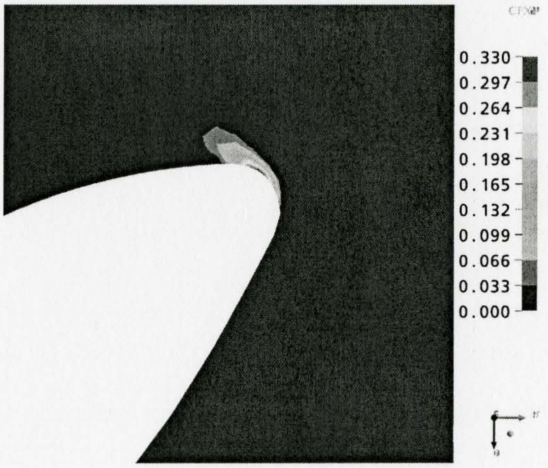

(b) $P_v = 1000$ Pa

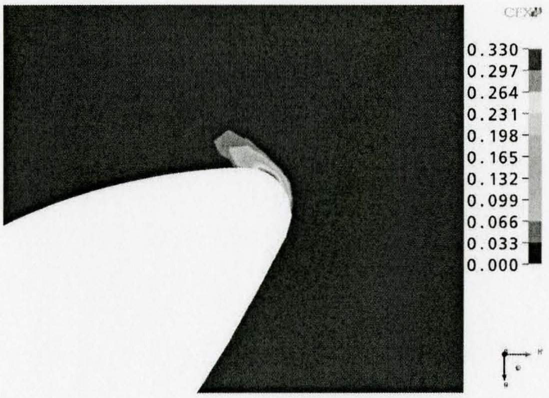

(c) P_v = 5000 Pa

Figure 3.15. Vapor volume fraction formation around the stator nose at a plane midway between the shroud and hub at pump speed of 2500 rpm and various vapor pressures using the default coefficients.

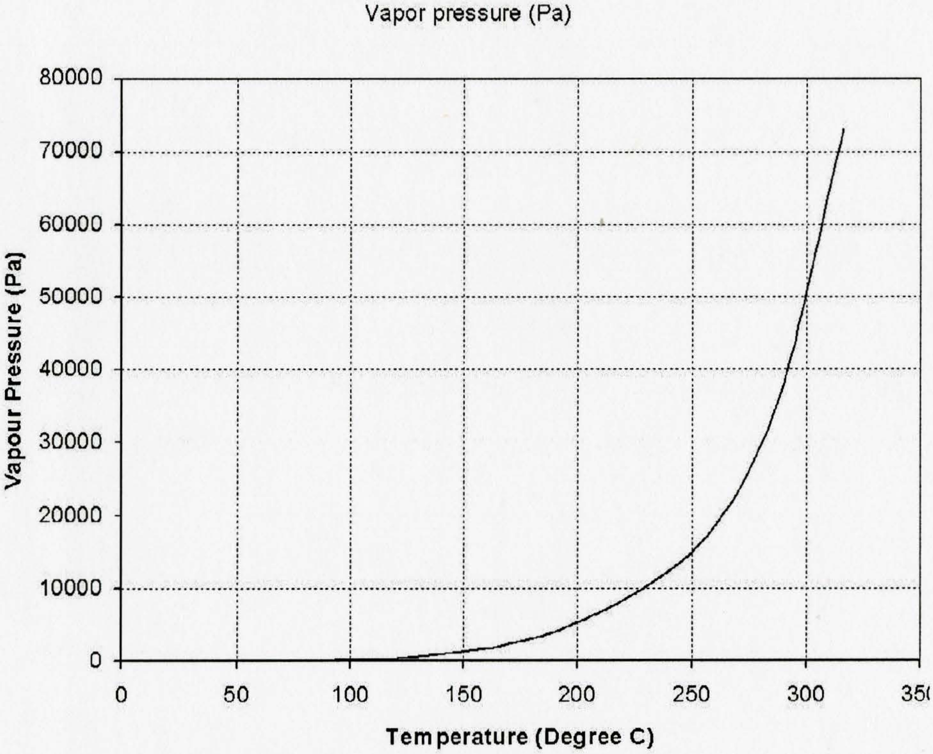

Figure 3.16. ATF vapor pressure Vs. temperature.

VVF at different pressures using the proposed empirical coefficients.

One set of simulations were carried out by using the proposed empirical coefficients using the k-ε model, at various vapor pressures. As we can see from the figure 3.17, changing the vapour pressure did not change the area of VVF, nor did it affect the K-factor (see figure 3.18.), which agrees with our previous study with the default values of the empirical coefficients.

This suggests that the empirical coefficients are the major factors in cavitation prediction. Proper value of vapor pressure should be chosen according to the experimental data, although it does not effectively affect the numerical results.

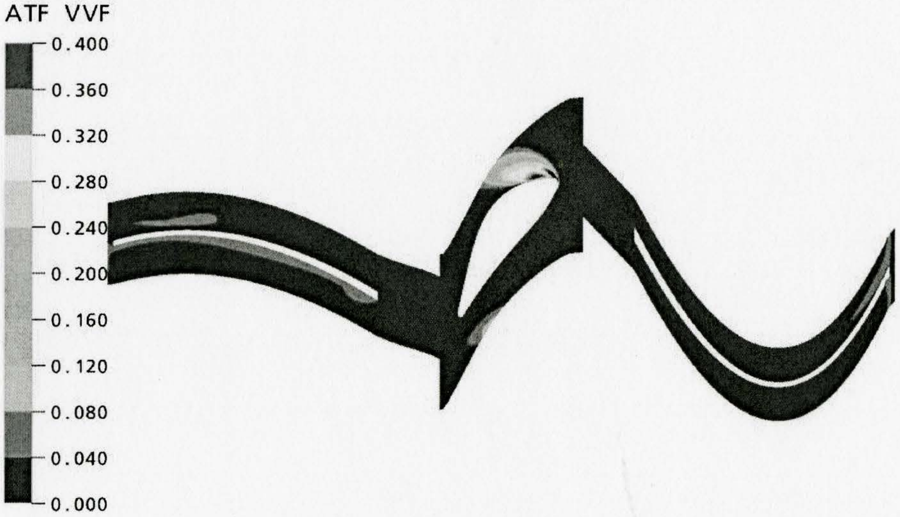

(a) P_v = 100 Pa

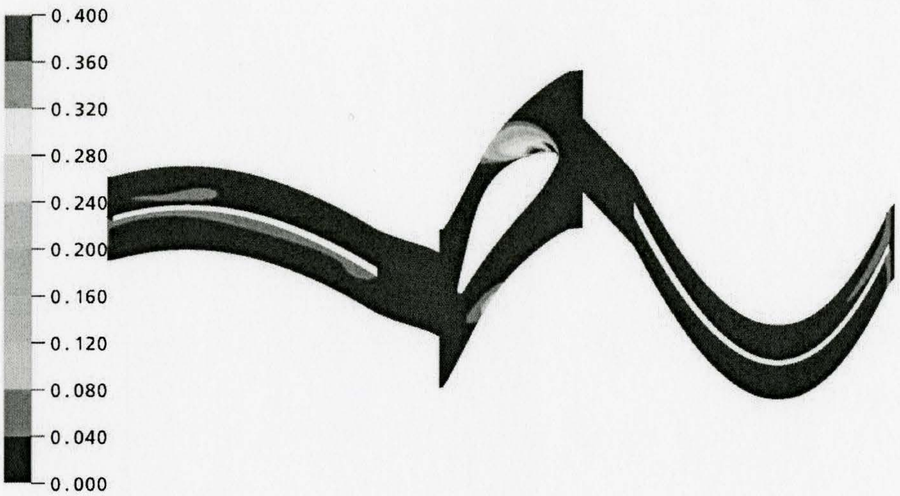

(b) $P_v = 1000$ Pa

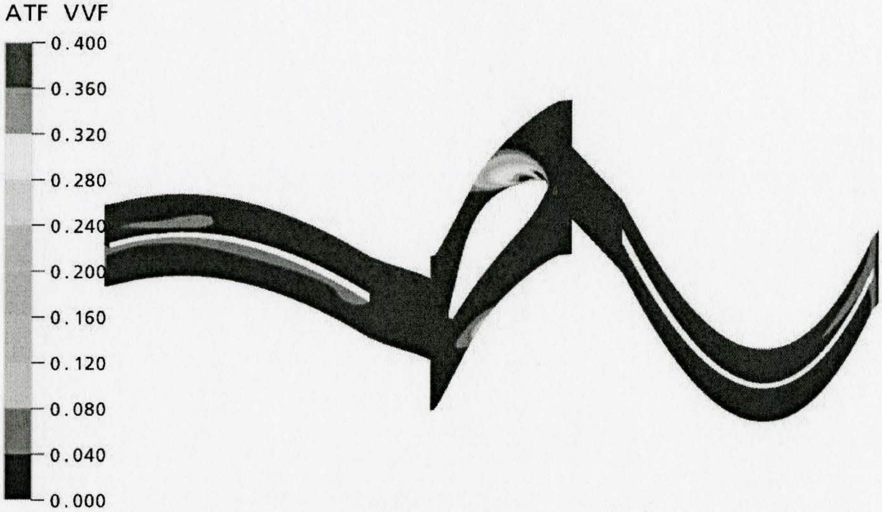

(c) $P_v = 5000$ Pa

Figure 3.17. Vapor volume fraction formation around the stator nose at a plane midway between the shroud and hub at pump speed of 2500 rpm and various vapor pressures using the proposed coefficients.

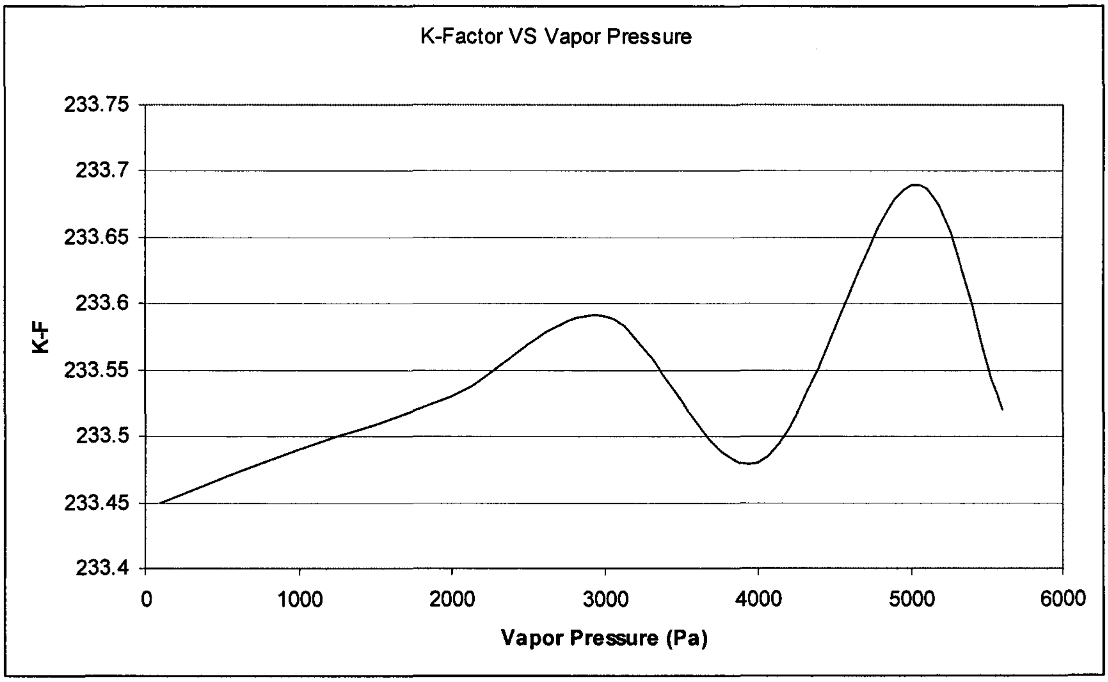

Figure 3.18. K-factor at various temperatures/vapor pressures using the modified coefficients.

3.2.4 Comparison between various turbulence models

3.2.4.1 Effects of turbulence models for the 310 mm TC (Results obtained from GM)

In GM's previous grant work, the standard k–ε turbulence model with standard wall function or scalable log law wall function was used in all cases. The standard k–ε turbulence model is only valid for high Reynolds number region of the turbulent flow field. Accordingly, it will introduce errors when applied to parts of the flow field, where the turbulent Reynolds number is low such as next to walls, although the scalable log law wall function attempts to minimize those errors. Another weakness of the standard k–ε model is that it is considered poor in predicting separated flows. In order to increase the simulation accuracy and to achieve the goal of this study, other turbulence models were studied in the present project. These include the k–ω model of Wilcox, the Shear Stress Transport (SST) model cast in the k–ω framework, the k–ε model of Kato and Launder, the standard Reynolds-stress (RS) model, and a modified RS model, with the Speziale-Sarkar-Gatski model (SSG). The k–ω model of Wilcox and the SST model can be applied to both the high and the low Reynolds number regions of the turbulent flow field. Thus, with these models, no wall functions are needed but a large number of grid points are needed in the near-wall region to resolve the flow features. For the k–ε model of Kato and Launder, it has a modified production term which gives more realistic estimate of generation of turbulence kinetic energy, where the flow stagnates. The Reynolds-Stress turbulence model (RSM), which solves six transport equations for each of the Reynolds stress and a transport equation for the length scale, is the most sophisticated model possible. RSM can account for effects of rotation and streamline curvature on turbulence in a natural way. The RSM used in this study is only valid for the high Reynolds number region of the flow field so wall functions are needed next to walls.

Table 3.1 shows a comparison of results obtained by using the several turbulence models. From this table, it can be seen that the k – ω of Wilcox model gives the best result. By using this model, the difference between the CFD prediction and the experimental measurement dropped to 12.2% from previous 17.1%. No other models, including the RSM, were able to improve predictions in terms of torque ratios and/or K-factors. This indicates that the inability to properly account for rotation and streamline curvature in the turbulence model is not the main culprit for the inaccuracies.

To evaluate the effects of wall functions on the accuracy of CFD simulations, it is noted that the scalable log law wall function model was found to give a lower K-factor prediction, which implies an over prediction of the pump torque. This is unexpected since CFX-TASCFLOW claims the modified wall function could improve near-wall flow simulations. However, it was confirmed by simulations performed under both the previous and the current grants. To see if better results can be obtained without using wall functions, simulations were performed by using the SST model on a fine mesh. Table 3.2 shows the comparison of SST result with measured data at stall for 310mm TC. From this table, it can be seen that only minor improvements were observed made in the predictions even though wall functions were not used. This indicates that the use of wall function may not be the source of error.

	K-factor	Difference %
Exp data	94.2	0
Wilcox k – ω	89.27	5.52
k- ε – kato	91.34	3.13
Standard RSM, Standard wall function	90.84	3.70
Standard RSM, Scalable log law	82.33	14.42
SSG, Standard wall function	90.56	4.02

Table 3.1. Effects of turbulence models in predicting at stall for the 310 mm TC

	K-factor	Difference %
Exp data	94.2	0
SST	92.36	1.99

Table 3.2. Comparison of SST results with measured data at stall for the 310mm TC

3.2.4.2 Effects of turbulence models for the 245 mm TC

According to GM's work, three turbulence models were tested using the same fine mesh and our proposed empirical coefficients to determine the role of turbulence models in the cavitation prediction on the 245mm TC.

The k-ε model is known to be the most balanced model for its acceptable result accuracy and strong adaptability to most of the meshes and turbulence flows. Considering the cheap computational cost and the acceptable quality results, we used the k-ε model in most of our studies in this thesis. Comparing to the k-ε model, the k-ω model is in general more sensitive to the mesh inside the boundary layer, but tends to produce better results when the mesh is appropriate. Spalart-Allmaras model is a one equation model based on the turbulence eddy viscosity, which was originally developed for aerodynamic problems by Boeing. However, it is suggested that this model works very well with some turbulent machineries. Thanks to its simple mathematical formation, this model requires the least computational resource.

A single phase result without turning on the cavitation was used to accelerate the convergence. As shown in figure 3.19-3.21, all results showed some similarities as the main cavitation was formed around the nose of the stator, and some vapors could be seen over the pump blade extending to the inlet of turbine. However, in rest of the areas, the k-ω and S-A models predicted bigger vapor volume fractions, which did affect the flow transportation.

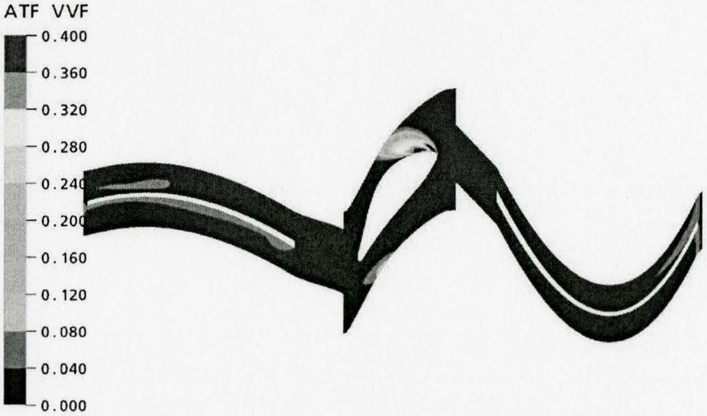

Figure 3.19. Vapor volume fraction in the pump, stator, and turbine at 2500 rpm pump speed – numerical results obtained using the proposed empirical coefficients using k-ε model.

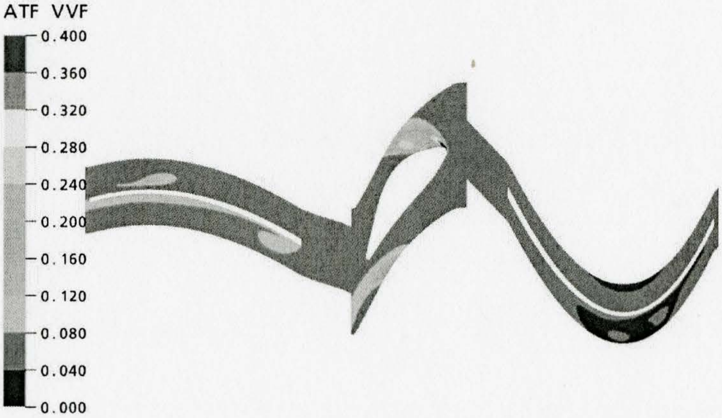

Figure 3.20. Vapor volume fraction in the pump, stator, and turbine at 2500 rpm pump speed – numerical results obtained using the proposed empirical coefficients using k-ω model.

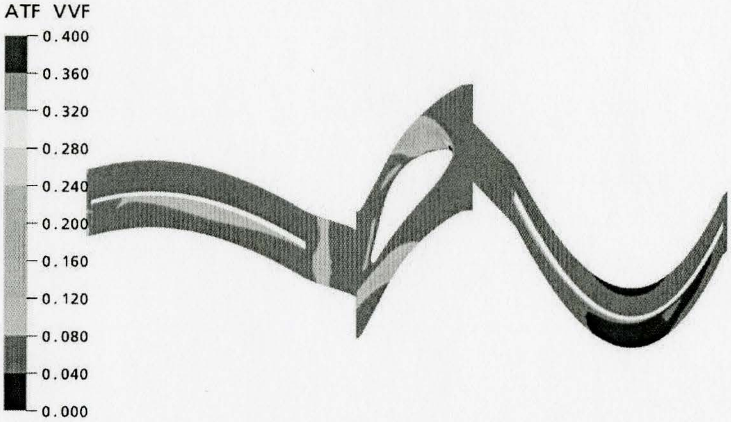

Figure 3.21. Vapor volume fraction in the pump, stator, and turbine at 2500 rpm pump speed – numerical results obtained using the proposed empirical coefficients using Spalart Allmaras model.

In comparison with the K-factor of 236 in the experiment, the K-factors computed by the k-ε, k-ω, and SA models were 233.7, 237.0, and 235.8 as shown in Table 3.3. All results were obtained using the same modified empirical coefficients, and the same vapor pressure of 5000 Pa.

We experienced that although the S-A model was the cheapest model computationally, it took the longest time to reach the convergence criteria at 1E-4, which may be caused by its mesh sensitivity; while the residues of the k-ε and k-ω models could reach 1E-5 in a much shorter time. After evaluating the result quality and convergence history, we found the k-ε model to be the most suitable model for our study.

	K-factor	Difference %
Exp data	236	0
Wilcox k – ω	237	0.4
k- ε	233.7	1
S-A	235.8	0.1

Table 3.3. Effects of turbulence models in predicting at stall for the 245 mm TC

3.2.5 Comparison between steady and unsteady simulations

3.2.5.1 Transient cavitation occurrence.

We proposed transient state because it could help us understand where and how cavitation takes place as a function of time. Promising results are shown in figure 3.22 for the cavitation occurrence using the k-ε model with the same proposed empirical coefficients as we found in the steady state. The time step was chosen to be 0.0001 second, and the total time was set to be 0.08 second.

Similar to what was observed in experiments, bubbles were mainly formed around the nose of the stator blades, and the vapor continued growing until it reached the free stream region and then being transported with the flow into the pump and further extended into the turbine. Some minor bubble formations were detected as well over the pump blades. Finally, bubbles almost covered everywhere in the torque converter, as which can be seen in figure 3.22.

Cavitation occurred remarkably fast, the K-factor increased from 222 (0 second) to 230 in just about 0.003 second; at about 0.015 second, a very similar picture was observed as our previous steady result; at 0.05 second, most of the regions have been covered by thin bubble clouds, a large VVF was accumulated above the nose of the stator blades, which was big enough to resist the torque transmission.

Additionally, it was found that the vapor pressure, again, could not affect the result in terms of the VVF and K-factor in the transient state. 5000 Pa was used as the vapor pressure in all the transient simulations.

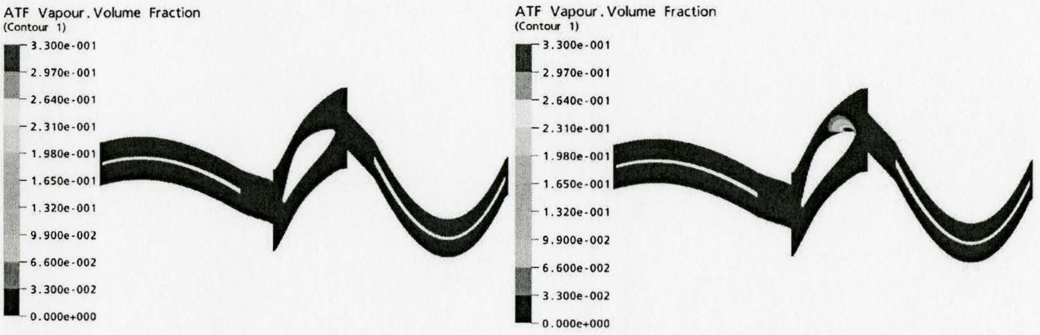

0second 0.0002 second

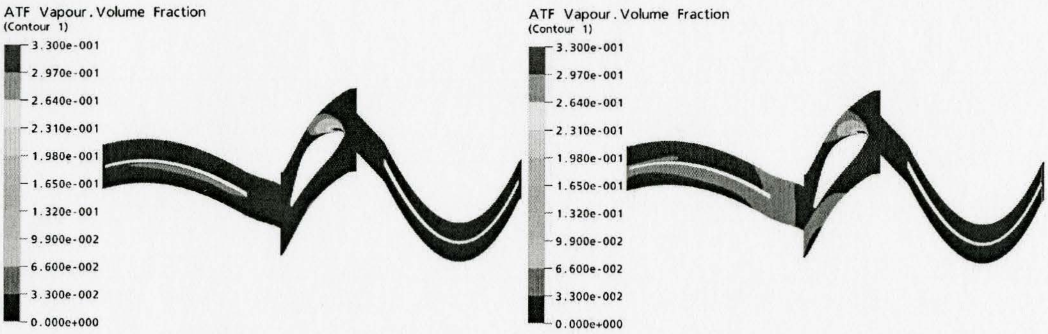

0.015 second 0.03 second

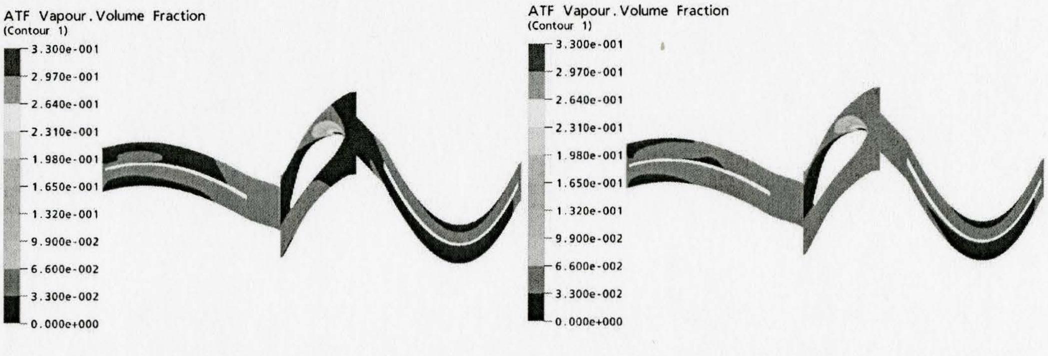

0.045 second 0.05 second

Figure 3.22. Vapor volume fraction at 2500 rpm pump speed –Transient vaporization results obtained using the proposed empirical coefficients at various time steps.

3.2.5.2 Comparison between steady and transient results

Figure 3.23 shows how K-factor varies with simulation type and time. Two sets of modified coefficients were used in both steady and transient states, which are $C_{vap}=500, C_{cond}=0.01$ and $C_{vap}=1\times10^{-6}, C_{cond}=50000$. We used the k-$\varepsilon$ turbulence model in all the transient simulations with the same vapor pressure of 5000pa.

As time goes on, the K-factor in the transient state increases and then tends to remain at certain levels after several time steps. It is worth noting here that the K-factor in the steady state appears to be the time averaged value of the K-factor in the transient state.

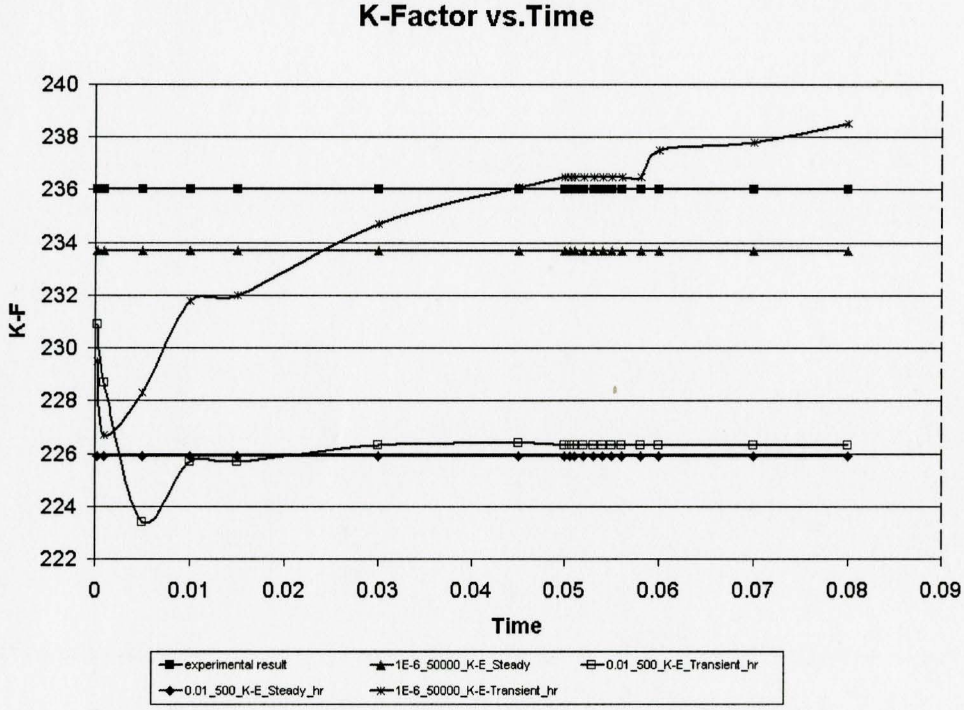

Figure 3.23. A comparison of K-factors obtained from both steady and transient states using k-ε model at various time steps.

As we mentioned in the part of steady state results, choosing "upwind" as the advection scheme instead of "high resolution" will lead to an increase of the K-factor. This was again observed in transient state as shown in figure 3.24.

We took the pair of results that both using C_{vap}=500, C_{cond}=0.01 as an example here. The K-factor predicted using "high resolution" finally remained at about 226 while the one predicted using "upwind" arrived at about 232, however, without any noticeable increase in terms of VVF shown in figure 3.25. Therefore, CFX10.0 over predicted the K-factor again in the transient state when using "upwind" as the advection scheme which made no sense physically.

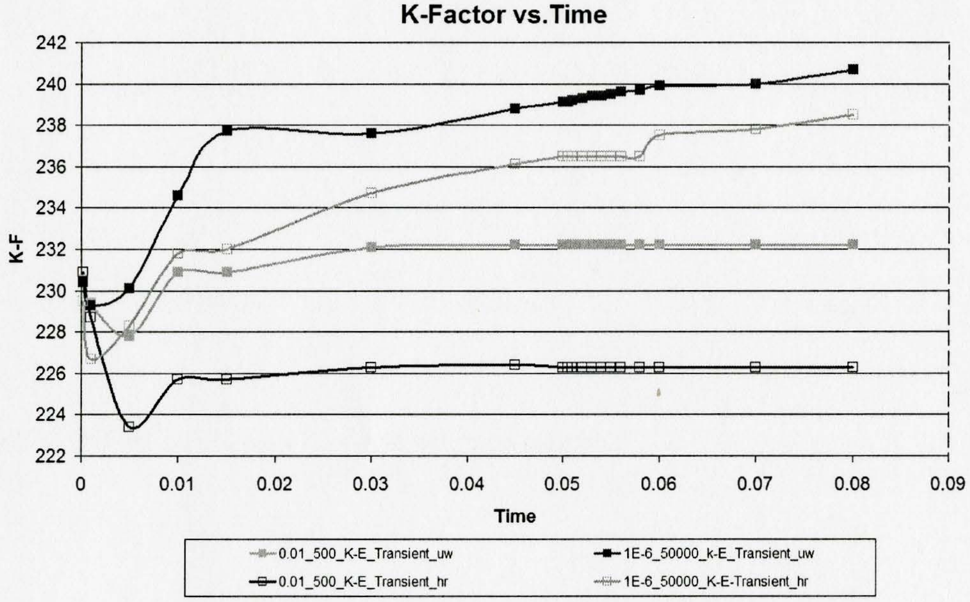

Figure 3.24. K-factors obtained by using different advection schemes with modified coefficients in the transient state.

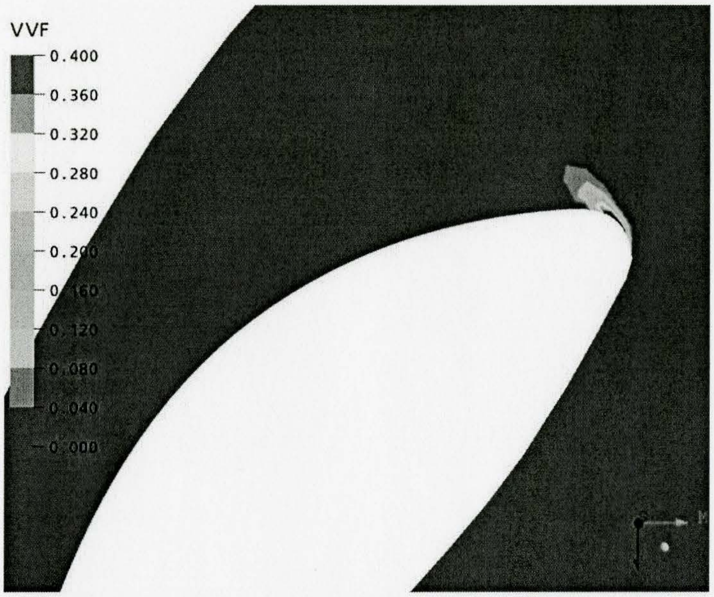

(a) Using high resolution

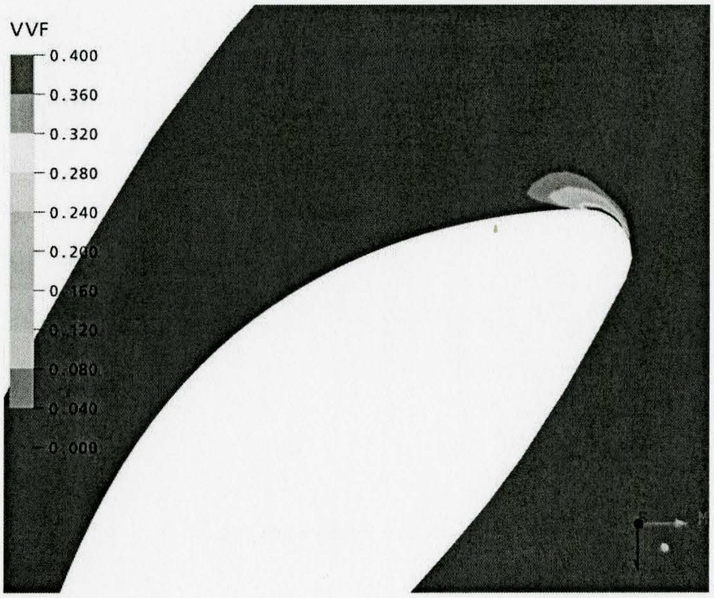

(b) Using upwind

Figure 3.25. Vapor volume fraction at 2500 rpm pump speed – transient numerical results obtained using the same modified coefficients and different advection schemes.

Chapter 4 Conclusion and Future Work

4.1 Research methodology overview

The research procedure can be expanded into five sections, as shown below:

(1) Validation of 3D model

The 3D models of 245mm and 258mm torque converters were obtained from GM for our numerical study. Before starting our research, numbers of simple simulations on these two models were carried out, to compare with experimental results, in order to validate the usability of these models.

(2) Validation of mesh

After validating the models, the right size of mesh for our future studies needed to be determined. The size of mesh is very critical in numerical simulations. Finer mesh leads to more accurate result, but costs significantly more computationally. Hence, three different sizes of mesh were made and several simulations were carried out respectively, to optimize the balance between accuracy and computational cost.

(3) Proposing three modified empirical parameters

After choosing the right mesh, several simulations with the implemented cavitation model in CFX10.0/11.0 were carried out by using default values. However, the results showed very limited volume of bubbles, which could not virtually affect the flow transportation. Hence, modifications were needed to apply to three key parameters, which are condensation coefficient, vaporization coefficient and vapor pressure. A large number of simulations have been carried out to determine the right modification, and during the same time, the effects of these three key parameters have been determined. Using the proposed parameters, the numerical results showed a high degree of agreement with experimental results.

(4) The effect of turbulence models

In order to find out the effect of different turbulence models on the numerical results, several simulations were carried out to predict cavitation with different turbulence models using our previously proposed parameters. Considering the nature of fluid flow inside torque converters and the suitabilities of different turbulence models, we have chosen three turbulence models in our study, which are K-Epsilon model, K-Omega model, and Spalart-Allmaras model.

(5) Comparison between steady and transient state.

Last but not least, cavitation is an unsteady phenomenon; all of previous studies were carried out in steady state. In order to better understand the whole vaporization and condensation process of cavitation as a function of time, and the effect of using transient simulations, part of our previous studies were repeated in the transient state.

4.2 Conclusions

Several series of numerical simulations have been carried out to study cavitation inside hydrodynamic torque converters in both steady and transient states. The cavitation model used in the study is the one available in ANSYS-CFX 10.0/11.0 software package. Numerical simulations have been carried out using three grids (coarse, medium, and fine). The following conclusions can be derived out of the results obtained so far:

1. The numerical solution obtained using the coarse grid gave an incorrect result for torque converter performance parameters in the case of multi-phase flow, i.e., with cavitation.

2. The numerical solution obtained using the medium grid is very close to that obtained using the fine grid. So, the medium grid has been regarded as sufficient.

3. Results from the numerical simulations employing the cavitation model developed by Zwart et al. (2004) did not agree with the experimental performance parameters, i.e., the K-factor and the torque ratio. The numerical results showed the formation of small areas of vapor over the stator nose. These areas did not have any significant effect on torque converter performance parameters.

4. The default values of the empirical coefficients of the current cavitation model need to be tuned, which has already been suggested and implemented by Zwart et al. (2004) when they tried to use their model to simulate cavitation inside a venturi, as mentioned previously.

5. After a large number of attempts, we successfully arrived at a good pair of value of model coefficients which helped us fully capture cavitation occurrence in the steady state. Comparing to the experimentally determined K-factor of 236, the one we obtained from our simulation was 233.7. The vapor volume fraction observed in our simulation was considerably remarkable to resist the torque transmission. Our proposed empirical coefficients for the 245mm torque converters are C_{vap} =50000 and $C_{cond} = 1\times10^{-6}$, which were tuned from the default values of C_{vap} =50 and

C_{cond}=0.01.

6. We evaluated the effects of using three different turbulence models which are the k-ε model, the k-ω model and the Spalart-Allmaras model. We finally chose the k-ε model as the most suitable model in our study by evaluating the balance between efficiency and accuracy.

7. Several simulations in the transient state have been carried out to study where and how cavitation occurs as a function of time. A remarkably fast bubble growth and transportation was observed within only 0.08 second. We captured and analyzed the time dependent K-factor, which agrees well with our previous observation in the steady state and the experimental data.

8. We also applied different values of vapor pressure in both steady and transient state, before and after tuning the empirical coefficients. The conclusion was the vapor pressure could not effectively affect the computation of the K-factor, nor did it affect the vapor volume fraction. The effect of vapor pressure is neglectable comparing to the effect of the other two empirical coefficients: C_{vap} and C_{cond}.

9. Using "upwind" advection scheme will lead to an over predicted K-factor or an under calculated pump torque, in both steady and transient state. However, it could not affect the computation of vapor volume fraction. Hence, choosing "high resolution" as the advection scheme is strongly recommended in the cavitation prediction.

4.3 Future work

Modifying the default values of the empirical coefficients of the existing model led to a better agreement between the numerical and the experimental results.

Although, modifying the model produced reasonable results, the fact that the values of empirical coefficients need to be tuned for every problem represents a significant obstacle in using the model, in another word, this pair of empirical coefficients vary with different geometries. Therefore, an alternative cavitation model without complex empirical coefficients is needed. In order to achieve a more precise prediction, the new cavitation model should take into account the complete Rayleigh-Plesset equation for bubble dynamics which includes the effect of viscosity and surface tension, we also want to investigate the effect of having slip between two phases.

References

Abe, K.I., Kondoh, T., Kagenori, F. and Kojima, M., 1991, "Threedimensional simulation of the flow in a torque converter," SAE paper No. 910800.

Anderson, C.L., Zengand, L., Sweger, P.O., Narain, A. and Blough, J.R., 2003, "Experimental investigation of cavitation signature in an automotive torque converter using a microwave telemetry technique," The International Journal of Rotating Machinery, vol. 9, no. 6, pp. 403–410.

Bai, M., Fiebig, L. and Mitra, N.K., 1997, "Numerical analysis of turbulent flow in fluid couplings," Transactions of the ASME, Journal of Fluids Engineering, vol. 119, pp. 569–576.

Bakir, F., Rey R., Gerber, A.G., Belamri T. and Hutchinson, B., "Numerical and experimental investigations of the cavitating behavior of an inducer," 2004, Interantional Journal of Rotating Machinery, vol. 10, pp. 15–25.

Brennen, C.E., 1995, "Cavitation and Bubble Dynamics," Oxford University Press, New York.

Brun, K. and Flack, R. D., 1997, "Laser velocimeter measurements in the turbine of automotive torque converter: Part I- average measurements," Transactions of the ASME, Journal of Turbomachinery, vol. 119, pp. 646–654.

Brun, K., Flack, R. D. and Gruver, J.K., 1996, "Laser velocimeter measurements in the pump of an automotive torque converter: Part II- unsteady measurements," Transactions of the ASME, Journal of Turbomachinery, vol. 118, pp. 570–577.

By, R.R. and Kunz, R., 1995, "Navier-Stokes analysis of the pump flow field of an automotive torque converter," Transactions of the ASME, Journal of Fluids Engineering, vol. 117, pp. 116–122.

Chen, Y.L. and Heister, S.D., 1995, "Two-phase modeling of cavitated flows," Computer and Fluids, vol. 24, no. 7, pp. 799–809.

Coutier-Delgosha, O., 2002, "Simulation of unsteady cavitation with a two-equation turbulence model including compressibility effects," Journal of Turbulence, vol. 3, pp. 1–20.

Davidson, L., 2003, "An Introduction to Turbulence Models," Report. 97/2, Dept. of

Thermo and Fluid Dynamics, Chalmers University of Technology, Göteborg.

Dong, Y., Korivi, V., Attibele, P. and Yuan, Y.Q., 2002, "Torque converter CFD engineering part I: torque ratio and K factor improvement through stator modification," SAE Technical Paper Series No. 2002-01-0883.

Dong, Y., Korivi, V., Attibele, P. and Yuan, Y.Q., 2002, "Torque converter CFD engineering part II: performance improvement through core leakage flow and cavitation control," SAE Technical Paper Series No. 2002-01-0884.

Dongan, Y., Lakshminarayana, B. and Maddock, D.G., 1998, "Steady and unsteady flow field at pump and turbine exits of a torque converter," Transactions of the ASME, Journal of Fluids Engineering, vol. 120, pp. 538–548.

Hammitt, F.G., 1980, "Cavitation and Multiphase Flow Phenomena," McGraw Hill Inc.

Ivany, R.D. and Hammitt, F.G., 1965, "Cavitation bubble collapse in viscous compressible liquids- numerical analysis," Journal of Basic Engineering, vol. 87, pp. 977– 985.

Lee, C.W., Jang, W.J., Lee, J.M. and Lim, W.S., 2000, "Three dimensional flow field simulation to estimate performance of a torque converter," Society of Automotive Engineers, vol. SAE No. 2000-01-1146, 2000.

Mekkes, J., Anderson, C. and Narain, A., 2004, "Static pressure measurements and cavitation signature on the nose of a torque converter's stator blades," to be published at International Journal of Rotating Machinery.

Menter, F.R., 1994, "Two-equation eddy-viscosity turbulence models for engineering applications," AIAA Journal, Vol. 32, No. 8, pp. 1598-1605.

Marathe, B. V., Lakshminarayana, B. and Maddock, D. G., 1997, "Experimental investigation of steady and unsteady flow field downstream of an automotive torque converter turbine and inside the stator: Part II- unsteady pressure on the stator blade surface," Transactions of the ASME, Journal of Turbomachinery, vol. 119, pp. 634–645.

Ofria, C., 2000, "How a transmission works," How Your Transmission Works, http:// www.mrtmilex.com/mrthowitworks.htm.

Poritsky, H., 1951, "The collapse or growth of a spherical bubble or cavity in a viscous fluid," Proceedings of the 1951 International Congress of Mathematics, pp. 813–821.

Schulz, H., Greim, R. and Volgmann, W., 1996, "Calculation of three-dimensional viscous flow in hydrodynamic torque converters," Transactions of the ASME, Journal of Turbo machinery, vol. 118, pp. 578–589.

Schweitzer, J. and Grandham, J., 2003, "Computational fluid dynamics in torque converters: validation and application," International Journal of Rotating Machinery, vol. 9, pp. 411–418.

Shin, S.H., Chang, H.J. and Joo, I.S., 2000, "Effect of scroll angle on performance of automotive torque converter," SAE 2000-01-1158.

Shu, S.S., 1951, "Note on the collapse of a spherical cavity in a viscous incompressible fluid," Proceedings of the 1951 International Congress of Mathematics, pp. 823–825.

Singhal, A.K., Athavale, M.M., Li, H.Y. and Jiang,Y., 2002, "Mathematical basis and validation of the full cavitation model," Journal of Fluids Engineering, vol. 124, pp. 617– 624.

Spalart, P.R. and Allmaras, S.R., 1992, "A One-Equation Turbulence Model for Aerodynamic Flows," AIAA Paper 92-0439.

Tennekes, H., and Lumley, J., 1972, "A First Course in Turbulence," The MIT Press, Cambridge, Massachusetts.

Von Backstrom, T. W. and Lakshminarayana, B., 1996, "Perspective: Fluid dynamics and performance of automotive torque converters: An assessment," Transactions of the ASME, Journal of Fluids Engineering, vol. 118, pp. 665–676.

Wilcox, D., 1988, "Reassessment of the scale-determining equation," AIAA Journal 26, vol. 11, pp.1299–1310.

Wilcox, D., 1993, "Turbulence Modeling for CFD," DCW Industries, Inc., 5354 Palm Drive, La Canada, California 91011.

Yves, L., 1999, "Cavitation Bubble Trackers," A. A. Balkema Publishers.

Zeng, L., 2000, "Experimental Investigation of Cavitation Signatures in an Automotive Torque Converter," Master's thesis, Michigan Technological University.

Zwart, P.J., Gerber, A.G., and Belamri, T., 2004, "A two-phase flow model for predicting cavitation dynamics," in "ICMF 2004 International Conference on Multiphase Flow," Yokohama, Japan.